NTNU

Norwegian University of
Science and Technology

Tidal and Wind Driven Boundary Layer Flow in Coastal Zones

Ingrid Rolland Andersen

Marine Technology
Submission date: June 2018
Supervisor: Lars Erik Holmedal, IMT
Co-supervisor: Dag Myrhaug, IMT

Norwegian University of Science and Technology
Department of Marine Technology

Preface

This master thesis is written during the spring 2018 at the Department of Marine Technology at the Norwegian University of Science and Technology. The thesis completes a Master of Science in Marine Technology, with specialization within hydrodynamics.

The choice to write this paper within Oceanography was made during the spring 2017, when I took an elective course in Oceanography. I found the subject interesting, and I wanted to learn more about this field. Nature has always fascinated me academically, in addition to enjoying the outdoors on my spare time. As a part of the thesis I wanted to learn some basics within programming, since I had very little experience and knowledge regarding computational solvers.

Finishing this thesis, I am left with an increased understanding of how the major forces in nature interacts. Performing the simulations of the different flows have been a challenging, yet educational process. Using the model developed by Professor Lars Erik Holmedal to perform the simulations has been a suitable process to learn how the model works. To implement the effect of an increasing wind in the code required a further understanding of the model. Despite some trouble along the road, I am left with a high sense of achievement.

I would like to express my gratitude towards my supervisor Professor Lars Erik Holmedal for his guidance through the semester, and for providing me with the numerical model. I have always been welcome at his office, in addition he has been available by e-mail outside his office hours. I would also like to thank him for his patience with my learning process when developing my skills within programming. I would like to thank my co-supervisor, Professor Dag Myrhaug, for his contribution to my project thesis through guidance hours and sharing his expertise within oceanography. Finally, more thanks goes to PhD Candidate Jon C.Mossige, for patience and help when the numerical model became too complex.

June 11, 2018
Trondheim

Ingrid Rolland Andersen

Summary

The objective with this thesis is to investigate the start-up of a pure wind driven flow, and the effect of an suddenly increasing wind (starting from zero wind speed) on a tidally driven flow. This is done by performing simulations of a wind driven flow beneath a constant and an increasing wind, with no tidal forcing. Further, a pure tidally driven flow is simulated and a suddenly increasing wind is imposed when the tidal flow has obtained steady state conditions. These simulations are compared with a fully developed flow beneath a constant wind with and without tidal forcing, respectively. For all cases the difference between imposing a strong and weak wind on the flow is also accounted for. Studying the tidally driven flow beneath an suddenly increasing wind starting at zero wind stress have, to the authors knowledge, not been done before. To predict the pure wind driven and combined tidal and wind driven flows a one-dimensional boundary layer model is applied. The horizontal velocities are calculated at 814 gridpoints in the vertical direction along the water column, with the highest resolution close to the sea bed and close to the sea surface where the flow is complex. A two-equation turbulence closure model is utilized to account for the turbulent flow.

Findings from the simulations of a pure wind driven flow showed that the particle trajectories beneath a weak wind is rotated further to the right relative to the direction of the wind stress, compared to a strong wind. This is assumed to be caused by the strong wind inducing more turbulence in the flow, which decreases the rotation of the surface Ekman current. This is consistent for the flow beneath a constant and a suddenly increasing wind. The particle trajectories in the flow beneath an increasing wind appears to move in a circular motion in the start-up of the simulation when the wind speed is low. This is especially seen for depths close to the sea bottom. The circular motion is similar to a trajectory only affected by the Coriolis force, and this may be caused by the inertia of momentum down in the water column. The Coriolis force is proportional to the horizontal velocities u, v and the shear force to the velocity gradients $\frac{du}{dz}, \frac{dv}{dz}$, and the results implies that the Coriolis force dominates over the shear force when the horizontal velocities are small and there is no tidal current.

The velocity profiles for the combined tidal and wind driven flow shows little difference in the speed compared to the velocity profiles for a pure tidally driven flow. This implies

that the tidal current is dominating the velocity in the flow, and the effect from the wind on the horizontal velocities are mostly limited to the flow close to the ocean surface.

The direction of the mass transport (drift) through the water column in a combined tidal and wind driven flow varies for a flow beneath a constant and a suddenly increasing wind, despite the same resulting wind speed. This is likely to be caused by the difference in wind speed in the start-up of the simulation, were the constant wind induces a drift rotated further to the right relative to the direction of the wind speed, compared to the increasing wind. These results consist with the Coriolis force being proportional to the horizontal velocities u, v in the flow, where an increased magnitude of u, v results in a higher effect of the Coriolis force rotating the trajectories beneath a constant wind to the right compared to the direction of the wind. The flow beneath an suddenly increasing wind will have lower horizontal velocities and the trajectories are not affected of a Coriolis force of the same magnitude as the flow beneath a constant wind.

In conclusion, the effect of an increasing wind on the flow is different than the effect of a constant wind. The presence of a tidal flow results in turbulent mixing which reduces the difference due to little inertia of momentum down in the water column, but e.g the direction of drift beneath an increasing wind deviates compared to the drift in a flow beneath a constant wind. In exposed seas as e.g the North Sea transient winds may be more relevant compared to steady state conditions, and the knowledge about these types of winds should be investigated further. For further work it could be interesting to compare the difference of a tidally driven flow beneath a wind increasing exponentially or with another ramp than linear, which is applied here. The effects of surface waves due to the wind should also be investigated further in order to predict a sea state as realistic as possible.

Sammendrag

Målet med denne oppgaven er å undersøke oppstarten av en vinddrevet strømning, og hvordan en plutselig økende vind påvirker en tidevannsstrømning. Dette er gjort ved å utføre simuleringer av en vinddrevet strømning under en konstant og en økende vind, som ikke er påvirket av tidevann. Videre er det gjort simuleringer av en fullt utviklet tidevannsstrømning hvor effekten av en plutselig økende vind er påført i overflaten. Disse simuleringene ble sammenlignet med en fullt utviklet strømning under en konstant vind, med og uten effekt av tidevann. For å simulere dette er det brukt en en-dimensjonal grenselagsmodell, utviklet av Holmedal (2002). De horisontale hastighetene er beregnet ved 814 punkter i vertikal retning fra havbunn til havoverflate. Punktene er plassert tettest nærmt havbunn og i overflaten, hvor strømningen er kompleks. Det er benyttet en turbulent slutningsmodell med to ligninger. Funn fra simuleringen av en vinddrevet strømning uten tidevann viser at partikkelbanene under en svak vind roteres lengre mot høyre i forhold til vindretningen, sammenlignet med partikkelbanene under en sterk vind. Det er antatt at dette skyldes at en sterk vind over havet induserer en mer turbulent strømning og at dette påvirker havet ved at vannlagene i overflatestrømmen roteres mindre i forhold til hverandre. Dette stemmer også for en svak og sterk økende vind over en strømning uten tidevann. Partikkelbanene i en strømning påvirket av en økende vind virker å bevege seg i en sirkulær bevegelse i vindens oppstart, da hastigheten til vinden er lav. Dette fenomenet er spesielt tydelig for partikkelbaner i vanndyp tett på havbunnen. Denne sirkulære bevelgelsen minner om en bane som kun er påvirket av Coriolis kraften, og dette kan skyldes en treghet av bevelgelser nedover i vanndypet. Coriolis kraften er proporsjonal med de horisontale hastighetene u, v i strømningen og skjærkreftene i strømningen er proporsjonale med hastighetsgradientene $\frac{du}{dz}, \frac{dv}{dz}$. Resultatet viser at Coriolis kraften dominerer over skjærkreftene når de horisontale hastighetene er lave og det ikke er noen tidevannsstrøm.

Hastighetsprofilene for en kombinert vind - og tidevannsstrøm viser liten forskjell i hastighetene sammenlignet med en ren tidevannsstrømning. Dette antyder at tidevannsstrømningen dominerer hastighetene over hele vanndypet, og at effekten fra vind er begrenset til lagene tett på overflaten.

Retningen til massetransporten i vanndypet i en tidevannsstrøm varierer under en konstant vind og en økende vind, til tross for at den resulterende vindhastigheten er den samme. Dette skyldes sannsynligvis forskjellen i vindhastighet i starten av tidevannssyklusen, hvor den konstante vinden fører til en massetransport som er rotert lengre mot høyre i forhold til retningen til vindhastigheten, sammenlignet med massetransporten under en økende vind. Resultatene sammenfaller med at Coriolis kraften er proporsjonal med de horisontale hastighetene u, v i strømningen, hvor en økende hastighet av u, v vil resultere i en større påvirkning fra Coriolis kraften og strømningen roteres mot høyre relativt til vindretningen. Strømmen under en plutselig økende vind vil ha lavere horisontale hastigheter og strømningen her er derfor ikke påvirket av en like stor Coriolis kraft.

Det kan konkluderes med at massetransporten lokalt i vanndypet varierer om strømmen er påvirket av en konstant vind eller en økende vind. Tilstedeværelsen av en tidevannsstrøm fører til turbulent blanding av sjøen, og dette reduserer forskjellen som følge av treghet i bevegelser nedover vanndypet. Resultatene viser at retningen til massetransporten under en økende vind avviker sammenlignet med massetransporten under en konstant vind. I utsatte sjøområder som for eksempel Nordsjøen, kan flyktige vindkast være mer relevant enn stabile forhold, og derfor burde kunnskapen om hvordan disser vindene påvirker sjøen økes. For framtidig arbeid vil det være interessant å undersøke tidevannsstrømmen under en vind som øker eksponensielt, og ikke bare linært som er benyttet her. Effekten av bølger i overflaten som følge av vind burde også undersøkes nærmere for å forutsi en sjøtilstand så realistisk som mulig.

Contents

List of Figures

List of Symbols

ρ	Density of a fluid
$\vec{\Omega}$	The angular velocity of the Earth-Moon system
$\vec{\omega}$	The Earth's angular velocity
$\vec{\rho}$,ρ	Vector between a point P on the Earth's surface and the Moon's centre of mass, Length of vector $\vec{\rho}$ in Section 2.1
$\vec{a_E}$	The acceleration of origo in a relative system
$\vec{a_T}$	Motion around the Sun
$\vec{a_{P,abs}}$	The absolute acceleration of a point P
$\vec{a_{P,rel}}$	The acceleration of a point P in a relative system
$\vec{G}$	Gravitational force from the Moon working on a point P on the Earth
$\vec{r_P}$	Position of P in a relative system
$\vec{r_E}$	Vector between the Earth's and the Moon's center of mass
$\vec{S_0}$	The centrifugal force
$\vec{T}$	The tide-producing force
$\vec{v}_{P,rel}$	The velocity of a point, P, in a relative system
k	Kinetic turbulent energy

l_m	Length scale of the largest turbulent eddies
u, v, w	Velocities in x -, y - and w - direction.
u_g, v_g	Geostrophic velocity in x - and y - direction
δ	Kronecker delta function
ϵ	Dissipation rate
κ	Von Kárman constant
μ	Viscosity
ν	Kinematic viscosity
ν_T	Eddy viscosity
∂	Partial derivative
ρ_a	Density of air
ρ_w	Density of water
$\sum F$	Sum of forces
τ	Friction of a fluid
τ_s	Wind stress
τ_x, τ_y	Shear force in x - and y - direction
ζ	Amplitude of the surface elevation
c, $\sigma_k, \sigma_\epsilon, c_{\epsilon 1}, c_{\epsilon 2}, c_1$	Model constants
C_D	Sea surface drag coefficient
c_d	Friction factor
d	The Ekman depth

E	Roughness parameter
f	Coriolis parameter
f_0	Frequency of motion
F_τ	Shear force
F_c	Coriolis force
L	Length scale
M	Mass of the Moon
m	mass
p	Pressure
r	Radius of a circle
R_0	The Rossby number
Re	The Reynolds number
t	time
T_p	Tidal period
U_0	Free stream velocity
u_i	Velocities in x-, y- and z- direction for i =(1,2,3)
U_{10}	Mean wind speed at 10 meter elevation
U_τ	Resultant friction velocity
U_{res}	Resultant velocity parallel to a wall
V_m	Velocity scale of the largest turbulent eddies

x, y, z Coordinate system where x is positive towards the east, y is positive towards the north and z is positive upwards

y^+ Dimensionless wall distance

z_0 Sea surface roughness height

z_s Roughness at the ocean surface

Chapter 1

Introduction

The tides exist due to gravity forces from the Moon and the Sun working on the Earth, combined with relative motions of the Earth - Moon and Earth - Sun system. This leads to the rise and fall of the ocean level, and induces a tidal boundary layer when water is transported. This is referred to as the tidal currents. The tidal currents are important for transport of e.g. plankton, sea bottom material, waste and oil spill in the ocean. Recently, there has been an increasing focus in the media on plastic in the ocean. Similarly to the natural content of the sea, as plankton, the plastic is being transported with the major currents in the ocean until it flushes up on land. This is especially harmful for the wild life living in and by the sea, and in order to insert emergency measures it can be valuable to known how and where this is transported. In addition to transport of different ocean materials and waste, the tides can be of interest in design and operation of different offshore structures. Maritime technology is being continuously developed, and much indicates that the maritime industry will be even more important in the future.

Wind and ocean currents effect the velocity and mass transport in the ocean, and together with the tidal currents these are important phenomenons to consider when trying to predict the behaviour of the sea. The winds are, in opposite to the tidal currents, less predictable. The strength and direction of the winds can change suddenly and due to inertia of momentum down in the water column when the winds blow over the ocean surface, the flows beneath the winds are almost never fully developed. Haoliang, Malanotte-Rizzoli, Tieh-Yong, and Guiting (2014) investigated the importance of the wind driven and tidal circulations in a specific, coastal strait. They found that a strong wind forcing could be

of great importance for the circulation in coastal regions, even when the tides were strong and considered to be dominating.

The tidal currents create a boundary layer with the interaction of the sea bottom in shallow and intermediate water depths. The ocean-atmosphere interaction creates a boundary layer effecting the atmosphere and the ocean surface when a wind is blowing. From Ekman (1905) the effect of a constant blowing wind in the ocean surface is well known, and the interactions between a constant blowing wind and a tidally driven flow are known from studies as e.g. Holmedal and Myrhaug (2013). To the authors notice, the interaction between a tidal and wind driven flow where a sudden wind is imposed on the tidal flow has not yet been investigated. The objective with this thesis is to investigate the start-up of a pure wind driven flow, and the effect of an increasing wind (starting from zero wind speed) on a tidally driven flow. How strong and weak winds affects the flow will also be included. The results will be compared with the properties of a fully developed tidally and/or wind driven flow. As the flow within the boundary layer is turbulent by nature, a turbulence model is required to predict these flows. Provided that the turbulence is properly modelled, studies have shown that a relatively simple boundary layer model can be used to predict these flows (Holmedal and Myrhaug, 2013). Therefore, the same one-dimensional model with a two-equation turbulence closure developed by Holmedal (2002) and used in Holmedal and Myrhaug (2013) will be used to simulate the flow. Some modifications are applied in order to simulate the flow beneath an increasing wind.

In Chapter 2, 3 and 4 relevant background theory are presented. Chapter 5 gives a short description of the phenomenon turbulence, and how this can be taken into account in a numerical model. Chapter 6 describes the model used in this thesis, and the boundary conditions. The results from the present work are presented in Chapter 7, and discussed thoroughly. First, the results from a pure wind driven flow and a pure tidally driven flow are presented, before the results from a combined wind and tidally driven flow are discussed. In Chapter 8 a summary and conclusion are presented, and suggestions for future work are given in Chapter 9.

Chapter 2

Tides

The most familiar understanding of the tides are the rise and fall of the ocean level. The tide-generating forces leads to enormous masses of water being transported over large length scales in a regular pattern, each day. The tides are important for several processes in the ocean, and consist of more than just the visible changes in the ocean level. Governing forces of the tides are the gravitational forces from the Moon and the Sun, and a centrifugal force caused by the eccentric motion when the Earth-Moon system revolves around a common centre of mass. All masses are drawn to each other, and this causes a gravitational pull working on the other mass. The larger the mass, the larger the gravitational pull. In addition to size, the gravitational force depends on distance and decreases when the masses are far away from each other. This is why the gravitational force from the Moon has a larger effect on the Earth than the Sun. The interaction between the Earth and the Moon is important when understanding the changes in the tides (Pinet, 2016; Brown et al., 1989a). In this chapter two models used to explain the tides are described, with the effects of shallow waters and tidal currents. The Coriolis force is briefly presented, since this effect is important in order to understand the behaviour of the tides.

2.1 The Equilibrium Model

The equilibrium model is a common model used to explain the physics behind the tides. The model makes several assumptions, simplifying the "real world" (Pinet, 2016):

1. The Earth's surface is assumed to only consist of seawater of infinite depth, and there is no effect of the landmasses or the sea bottom.
2. The waves created by the tides are assumed to be progressive waves.
3. The seawater is assumed to be in equilibrium with the tide-producing forces at all times. In the equilibrium model the effect of the gravitational forces from the Sun are neglected. Since the Sun is 360 times further away from the Earth compared to the Moon, the tide-producing forces from the Sun is only 0.46 times that of the Moon. So despite the enormous mass of the Sun, the forces from the Earth - Sun system can be neglected to simplify the model (Pinet, 2016; Brown et al., 1989a).

The Earth-Moon system is considered to rotate about an axis, T through the system's combined center of mass. The acceleration of a fixed point P on the Earth's surface can be written as (Myrhaug, 2012):

$$\vec{a}_{P,abs} = \vec{a}_{P,rel} + 2\vec{\omega} \times \vec{v}_{P,rel} + \vec{a}_0 + \dot{\vec{\omega}} \times \vec{r} + \vec{\omega} \times \vec{\omega} \times \vec{r_P} \tag{2.1}$$

where $\vec{\omega}$ is the angular velocity of the Earth, $\dot{\vec{\omega}}$ is the angular acceleration of the Earth, $\vec{v}_{P,rel}$ is the velocity of point P in the relative system, $\vec{a_{P,rel}}$ is the acceleration of point P in the relative system, $\vec{a_E}$ is the acceleration of origo in the relative system and $\vec{r_P}$ is the position of P in the relative system. The two first terms on the right hand side are related to P's relative velocity, and is therefore zero when P is fixed to the Earth. The derivative of $\vec{\omega}$ is very small, i.e $\dot{\vec{\omega}} \times \vec{r} \approx 0$. The last term is normal to the Earth's axis, and does not contribute to tides since it does not vary. The remaining term can then be written

$$\vec{a}_{P,abs} = \vec{a}_E = \vec{a}_T + \vec{\Omega} \times \vec{\Omega} \times \vec{r}_E \tag{2.2}$$

where $\vec{a}_T$ is the motion around the Sun and can be neglected when the gravitational forces from the Sun are neglected. This gives

$$\vec{a}_{P,abs} = \vec{\Omega} \times \vec{\Omega} \times \vec{r}_E \tag{2.3}$$

The expression in Equation 2.3 consists of the Earth-Moon system's angular velocity, $\vec{\Omega}$. The system rotates about an axis through the Earth's and Moon's centre of mass denoted $\vec{r_E}$. This vector is the same at any location at the Earth since it goes through the Earth's centre of mass.

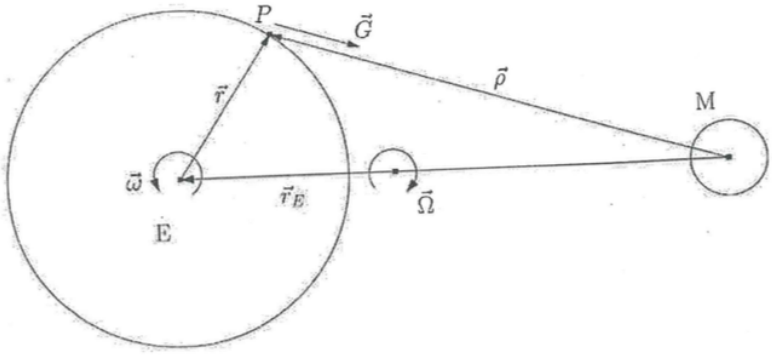

Figure 2.1: The Earth-Moon system. Illustration from Myrhaug (2012).

Inserted in Newton's second law, the equation becomes

$$\frac{\Sigma F}{m} = \vec{a}_{P,abs} = \vec{\Omega} \times \vec{\Omega} \times \vec{r}_E \tag{2.4}$$

$$\frac{\Sigma F}{m} - \vec{\Omega} \times \vec{\Omega} \times \vec{r}_E = 0 \tag{2.5}$$

The term $\vec{\Omega} \times \vec{\Omega} \times \vec{r}_E$ is considered as a force referred to as a centrifugal force. This force is equal at all points on the Earth. It should not be confused with the centrifugal force due to the Earth's spin around its own axis which increases with distance from the axis (Brown et al., 1989a). The centrifugal force discussed here is due to the eccentric motion when the Earth revolves about the Earth's and the Moon's common centre of mass. Consider a point on the Earth's surface. This point will follow a circular path due to the eccentric motion. The radius of the circular path will be the same for all points at the Earth's surface, and all points will experience the same angular velocity, and hence an equal acceleration and centrifugal force due to the eccentric motion (Brown et al., 1989a).

The gravitational attraction from the Moon working on a point P on the Earth, can be given by (Myrhaug, 2012):

$$\vec{G} = -G\frac{mM}{\rho^2}\frac{\vec{\rho}}{\rho} \tag{2.6}$$

where m is the mass of the Earth, M is the mass of the Moon, G is a gravitational constant, $\vec{\rho}$ is a vector from the centre of the Moon to a point P at the Earth's surface and ρ denotes the length of the vector $\vec{\rho}$. Since the distance between the Moon and the Earth depends on the location of point P, the position of point P will determine the magnitude of $\vec{G}$, i.e. the gravitational force from the Moon varies along the Earth's surface.

The centrifugal force is denoted:

$$\vec{S_0} = -m\vec{\Omega} \times \vec{\Omega} \times \vec{r}_E \tag{2.7}$$

This force is at equilibrium with the gravitational force, $\vec{G}$, at the Earth's center of mass. Since the centrifugal force is equal for all points at the Earth's surface and the gravitational attraction varies, the resultant force, $\vec{T} = \vec{S_0} + \vec{G}$, will vary. This is the only force contributing to the tidal range, and it is known as the tide-producing force. This force is directed into, parallel to, or away from the Earth's surface, depending on the position on the Earth's surface with respect to the Moon (Myrhaug, 2012; Brown et al., 1989a).

In Figure 2.2 the magnitude (not directly scaled) and direction of the tide-producing force for different points at the Earth's surface is shown with respect to the Moon. The Moon revolves around the centre of mass of the Earth-Moon system once every 27.3 days, in the same direction as the Earth moves around its own axis (once every 24 hours). Based on this, a lunar day is defined as 24 hours and 50 minutes which is the time between each time a point X on the Earth's surface is directly aligned underneath the Moon. The extra 50 minutes compared to the time the Earth uses to rotate once about it's own axis, is the time it takes the point X to "catch up" with the Moon, which has moved due to its rotation about the Earth. This is also the explanation to why the high tide at many locations is moved with almost an hour each day (Brown et al., 1989a).

Consider point E on the Earth's surface in Figure 2.2. Due to the Earth's rotation about its own axis, the tide-producing force will have following magnitude at point E during one turn (Myrhaug, 2012):

$$\begin{aligned}
\vec{T} &= \text{max} \quad \text{for} \quad \text{t} = 0 \quad \text{hours} \\
\vec{T} &= 0 \quad \text{for} \quad \text{t} = 6 \quad \text{hours} \\
\vec{T} &= \text{max} \quad \text{for} \quad \text{t} = 12 \quad \text{hours} \\
\vec{T} &= 0 \quad \text{for} \quad \text{t} = 18 \quad \text{hours} \\
\vec{T} &= \text{max} \quad \text{for} \quad \text{t} = 24 \quad \text{hours}
\end{aligned}$$

This results in two high tides and two low tides during 24 hours. Despite that the high tide is moved 50 minutes each day due to the rotation of the Moon and the Earth, the

tides are regular and can be predicted for the future, if they have been measured for the same place for a period of one year. How high and low the rise and fall will be varies locally, as it depends on the local geography of landmasses, depth and the shape of the sea basin (Pinet, 2016).

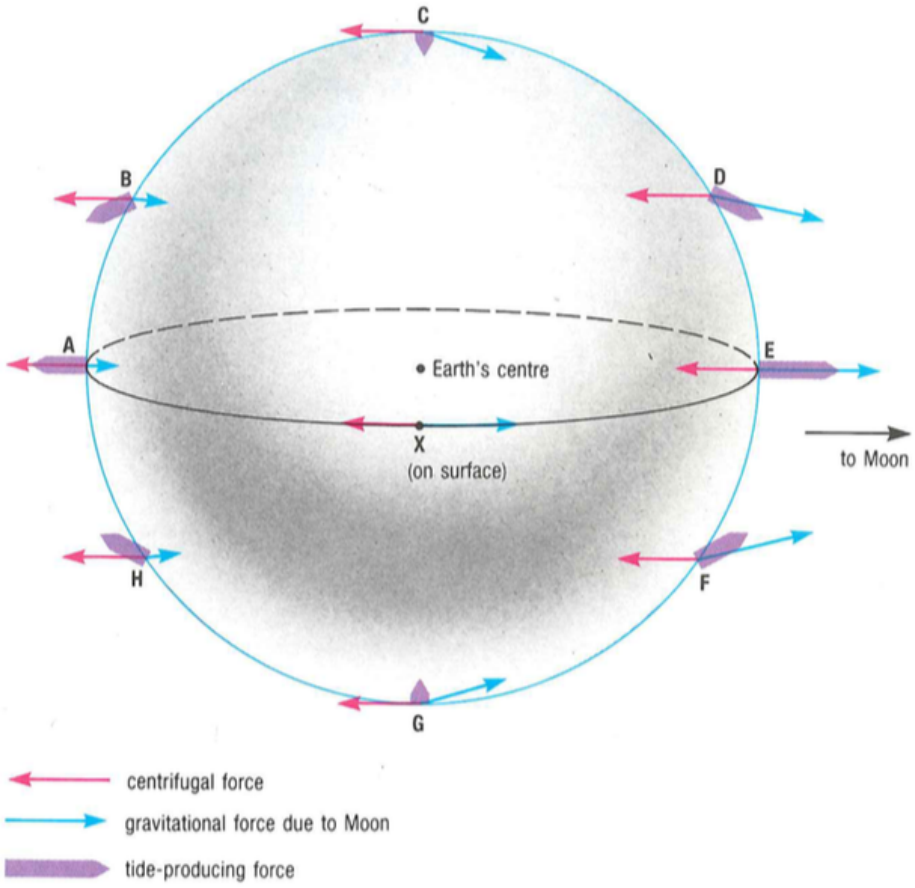

Figure 2.2: Tide-producing forces, gravitational forces and centrifugal forces on the Earth with respect to the Moon. Figure from Brown et al. (1989a).

2.1.1 Interaction of Solar Tides

As mentioned in the beginning of this section, the gravitational attraction from the Sun is about half of that of the Moon. When considering the interaction of a lunar and solar tide, the period between each time the Moon is aligned between the Earth and the Sun is considered as one cycle. Previously, it was mentioned that the high tide was postponed with 50 minutes each day due to the change in the Moon's position orbiting the Earth. Similarly, it takes the Moon 29.5 days between each time it is aligned directly between

the Earth and Sun. The Moon uses 27.3 days around the Earth meanwhile the Earth is also orbiting the Sun, i.e. the Moon needs the extra 2.2 days to catch up since the Earth's position around the Sun has moved. Every second week approximately, the Moon is positioned either aligned between the Earth and the Sun (new Moon) or the system is aligned from the left the Moon, the Earth and the Sun (full Moon), as seen in Figure 2.3. At these two positions the tide-producing forces from the Sun and the Moon are acting in the same direction, creating a high tide higher than normal. This is called spring tide, and occurs twice during the cycle of 29.5 days. When the Moon is in its first or last quarter as shown in Figure 2.3 the tide-producing forces from the Moon and the Sun is opposing, causing a low tide lower than normal. This is referred to as a neap tide (Brown et al., 1989a).

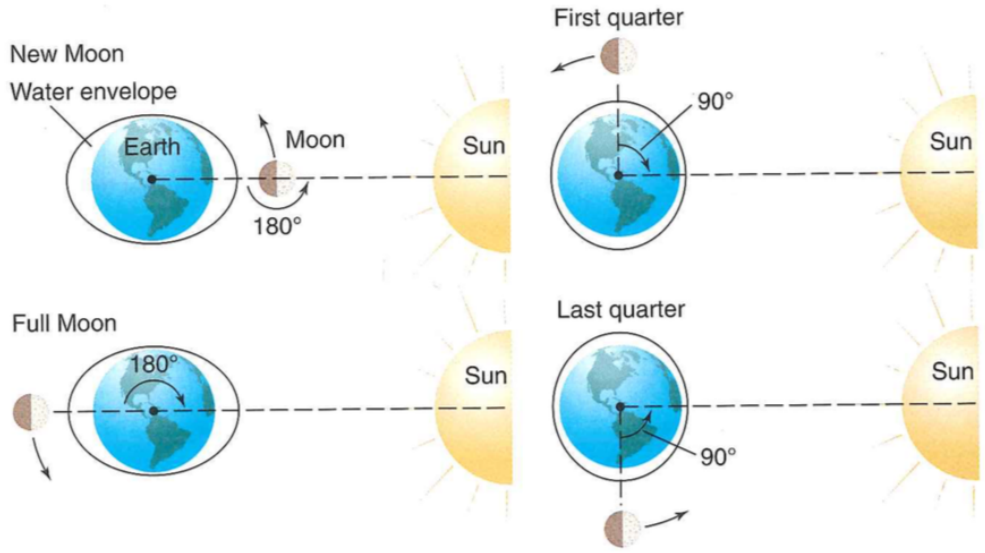

Figure 2.3: The figure shows the neap and spring tide as a result of the interaction between the lunar and solar tides. Figure from Pinet (2016).

2.2 The Coriolis Force

In order to properly explain how the tides behaves, the Coriolis effect must be understood. Consider Equation 2.1 from section 2.1

$$\vec{a}_{P,abs} = \vec{a}_{P,rel} + 2\vec{\omega} \times \vec{v}_{P,rel} + \vec{a}_E + \dot{\vec{\omega}} \times \vec{r} + \vec{\omega} \times \vec{\omega} \times \vec{r}$$

To explain the equilibrium model of the tides, this equation was considered for a particle fixed at the Earth's surface. Now consider a particle moving in the relative system. When neglecting the terms related to a fixed point at the Earth's surface, Equation 2.1 reduces to

$$\vec{a}_{P,abs} \approx \vec{a}_{P,rel} + 2\vec{\omega} \times \vec{v}_{P,rel} \tag{2.8}$$

where $\vec{a}_{P,rel}$ is the acceleration of P in a relative reference system, and $2\vec{\omega} \times \vec{v}_{P,rel}$ is the Coriolis-acceleration acting on P when it is moving with velocity $\vec{v}_{P,rel}$ in a relative reference system, with angular velocity $\vec{\omega}$ (Myrhaug, 2006). Implementing Newtons 2^{nd} law gives

$$\frac{\Sigma \vec{F}}{m} - 2\vec{\omega} \times \vec{v}_{P,rel} = \vec{a}_{rel} \tag{2.9}$$

An observer following a relative reference system will experience the term $2\vec{\omega} \times \vec{v}_{P,rel}$ as a force, though it is a fictive force. This effect of being in a rotating reference system will affect all motion on the Earth, including wind and currents. The physical meaning of this is that a particle will deflect with the Earth's rotation. In other words, in the Northern hemisphere, the Coriolis force is directed 90 ° to the right when looking in the direction of the motion (Myrhaug, 2006). A particle will therefore deflect to the right in the Northern hemisphere, as shown in Figure 2.4. In the Southern hemisphere, the Coriolis force is directed 90 ° to the left relative to the direction of motion. As shown in Figure 2.4, the particle deflects to the left. The magnitude of the Coriolis force varies locally on the Earth's surface, and the Coriolis effect has its maximum value at the poles, and is equal to zero at equator (Myrhaug, 2006).

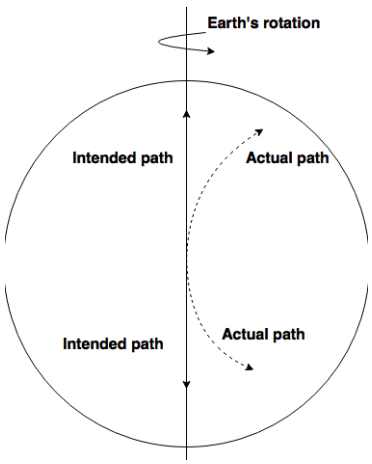

Figure 2.4: The figure shows the Earth, with the direction of motion (intended path) at the North and the South hemisphere, and how this path deflects due to the Coriolis effect.

2.3 The Dynamic Model of the Tides

Because of the simplifications made in the Equilibrium model of the tides, explained in Section 2.1, there are several properties of the tides that are not included in this model. To properly describe the behaviour of the tides, the effect of varying depth of the ocean basin and the presence of landmasses must be included. The water masses will move with an inertia compared to the rotation of the Earth, and this prevents the establishment of a equilibrium of the tides. Finally, the tide-producing forces are effected of the Coriolis force when the water is in motion (Brown et al., 1989a). Hence, a more accurate model to describe the tides is the dynamic model of the tides. Here, it is assumed that the oceans are dynamic, and responds actively to the tide-producing forces. The presence of landmasses is also taken into account in this model (Pinet, 2016).

The description of the dynamic model follows the explanation in Pinet (2016). Consider an ocean basin in the Northern hemisphere at the Earth, surrounded by landmasses at all edges. The ocean basin is uniform in depth and the effect of the Sun is neglected. When the Earth rotates towards the East, the water masses will be pressured at the West edge of the basin to remain in position beneath the Moon. As the rotation continues, more and more water is "splashed" against the West edge, until the pressure gradient becomes large enough and the water is tilted to the East in an attempt to counteract the pressure gradient. When the water is set in motion from West to East, it is influenced by the Coriolis effect, deflecting the motion to the right, and the water is pressured towards the South edge of the basin. In response to the piling water at the South edge, the water will flow towards the North, being deflected towards the East by the Coriolis effect. From East the water flows towards West to counteract the pressure gradient, and the flow is deflected to the North. From North the water flows towards the South, and the flow is again deflected and piled up against the East edge of the ocean basin, where the process started. When the water is pressured at the East edge, the process starts over again. The result is a rotating wave, consisting of a crest at the edges of the basin, and a trough in the middle. The crest represents the high tides, and the trough the low tides.

The tidal wave created by the constraints of the landmasses and the effect of the Coriolis force creates an amphidromic system. This is a system where the crest of the tidal wave rotates counterclockwise around an amphidromic point, once every tidal period. At the

amphidromic point the tidal range is zero, and the range increases at a line away from it (Brown et al., 1989a). In Figure 2.5 amphidromic systems in the North sea is shown. The red lines are called co-tidal lines, and define points within the same tidal range. The blue lines are called co-range lines, and they mark the point within the same amphidromic system that have the same tidal range. The numbers connected to the red lines indicate when the high tide occur, and it occurs at the same time of the day at every red line. Imagine that the crest of the tidal wave starts at zero hours, then all points connected to this line experiences the high tide at the same time of the day. For the points along the line marked one, experiences the high tide one hour later and so on. The hours are given in lunar hours, i.e. the one hours corresponds to 1/24 of a lunar day (Brown et al., 1989a; Pinet, 2016).

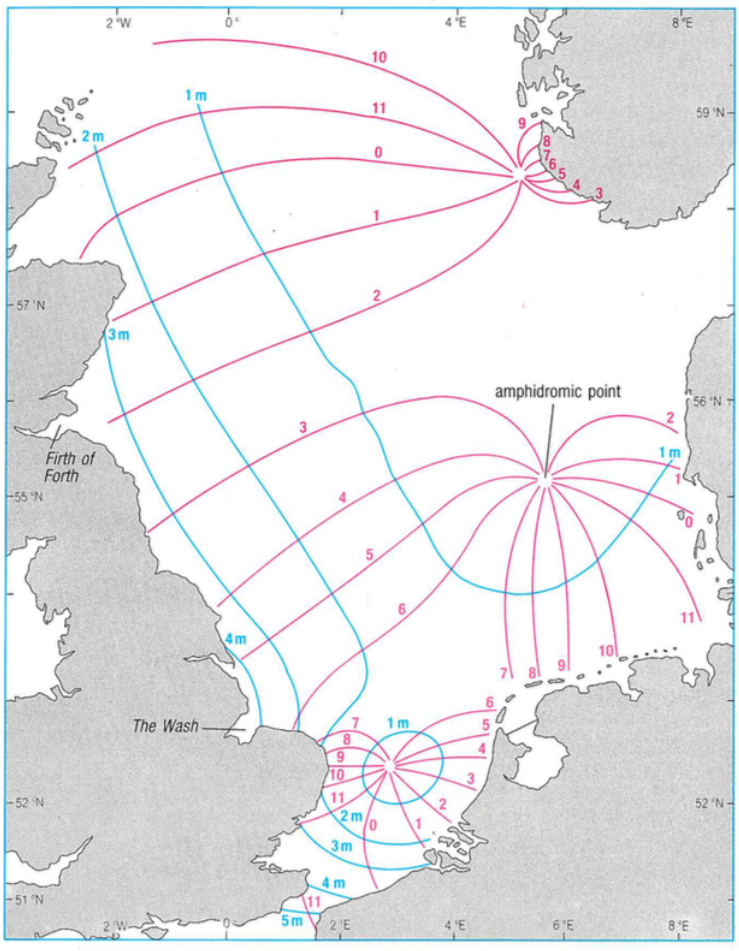

Figure 2.5: Amphidromic system's in the North Sea. Figure from Brown et al. (1989a).

2.3.1 Tidal Currents and the Effect of Shallow-waters

As described in Section 2.3, the tidal wave moves in a rotary wave within an amphidromic system, creating the rise and fall of the ocean surface. This vertical movement of the ocean surface is accompanied by horizontal water motion called the tidal current, moving with the same periodicity as the vertical movement (Brown et al., 1989a). These currents tends to follow an elliptical path as shown in Figure 2.6a.

In large and deep sea basins the effect of the sea bottom is negligible since the motion of the rotating wave only penetrates 0.5 wavelengths down in the water column (Faltinsen, 1990). However, in coastal areas with shallow water and a strong tidal current the effect of the sea bottom needs to be included. The frictional drag from the sea bed causes vertical shear and turbulent mixing in the bottom layers of the current. If the tidal current is weaker, stratification (water layers of different density) can occur (Brown et al., 1989a).

In Figure 2.6b vertical tidal current profiles are shown, where the frictional drag from the sea bed effects the velocity close to the sea bottom. The effect of turbulence and large scale motions such as the tidal currents will be further elaborated in Chapter 3 and 5.

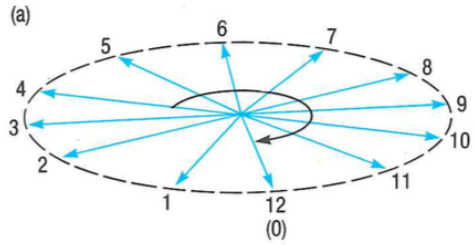

(a) The elliptical path followed by a water particle during a tidal cycle.

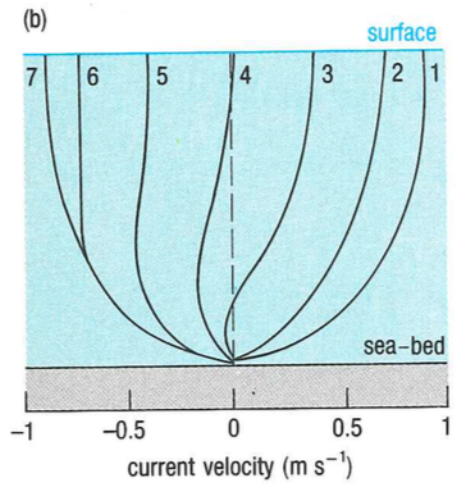

(b) Vertical tidal current profiles for half a tidal cycle. The numbers refer to time in lunar hours after an arbitrary start time.

Figure 2.6: Motions of the tidal current. Figures from Brown et al. (1989a)

Chapter 3

Boundary Layers

Boundary layers exits due to frictional forces when a fluid is flowing over a rough surface. As mentioned in Section 2.3, shear forces occur in the fluid when the tidal currents flow over the sea bottom, resulting in mixing of the fluid. Consider a fluid with low viscosity, μ, and very high Reynolds number flowing over a plate. The velocity close to the plate will be much smaller than at some distance from the plate. The no-slip condition states that the velocity of a particle directly on the plate is to be zero. The transition of the fluid from the plate and at a certain distance from the plate, where the velocity is unaffected of the plate, is called the boundary layer (Schlichting and Gersten, 2000). This transition exists due to shear stresses in the fluid. According to Newton's law of friction the fluid friction is given as

$$\tau = \mu \frac{\partial u}{\partial y} \tag{3.1}$$

where $\frac{\partial u}{\partial y}$ is the velocity gradient and μ is called the viscosity of the fluid. The viscosity is a physical property, and will vary with temperature and pressure. For a Newtonian fluid e.g. water, the relation between the velocity gradient $\frac{\partial u}{\partial y}$ and the shear stress τ is linear, as seen in Equation 3.1 (Schlichting and Gersten, 2000).

The Reynolds number, Re, of a fluid was defined by O.Reynolds in 1883 and describes the ratio of the inertial forces and viscous forces of a fluid flowing past a body, as shown in Equation 3.2 (Schlichting and Gersten, 2000):

$$Re = \frac{U_0 L}{\nu} \tag{3.2}$$

Here U_0 is the free stream velocity, L is the characteristic length of the body and ν the kinematic viscosity

$$\nu = \frac{\mu}{\rho} \tag{3.3}$$

with ρ as the density of the fluid. The flow is laminar for small Reynolds number, while for high Reynolds number, the acceleration term (inertia forces) is much larger than the viscous term (Myrhaug, 2012), and the flow becomes turbulent. This means that the high Reynolds number flow within the boundary layer is characterized by a chaotic flow with large velocity gradients.

3.1 Governing Equations

The boundary layer equations originate from the incompressible Navier-Stokes equations assuming a homogeneous, isotropic Newtonian fluid (Holmedal, 2002), with density ρ and kinematic viscosity ν. With incompressible flow, the density ρ can be assumed constant, and the continuity equation reduces to (Myrhaug, 2012)

$$\frac{\partial u}{\partial x} + \frac{\partial v}{\partial y} + \frac{\partial w}{\partial z} = 0 \tag{3.4}$$

By using Einsteins summation convention, with x_i(i=1,2,3)=(x,y,z) and u_i(i=1,2,3)=(u,v,w) where equal indices are repeated, the continuity equation can be written (Holmedal, 2002)

$$\frac{\partial u_i}{\partial x_i} = 0 \tag{3.5}$$

Correspondingly, the Navier-Stokes equations are given as

$$\frac{\partial u_i}{\partial t} + \frac{\partial u_i u_j}{\partial x_i} = -\frac{1}{\rho}\frac{\partial p}{\partial x_j} + \nu \frac{\partial^2 u_i}{\partial x_j \partial x_j} \tag{3.6}$$

The Navier-stokes equations completely describes the flow field of a fluid, but due to the complexity of the equations and the massive computational time required to solve them,

it is common to find simplified versions (Holmedal, 2002).

3.2 The Boundary Layer Equations

The boundary layer equations is a simplification of the Navier-Stokes equations, comparing the length scales for the application of the equations. For large scale motions, the vertical scale is much smaller than the horizontal scale. The deduction of the boundary layer equations from the Navier-Stokes equations is executed in Appendix A.

The Rossby number is used to determine whether Coriolis or inertia forces are dominating. Slow and large motions in the ocean i.e. the tides are an example of Coriolis dominated motion where the Coriolis term is important. When the inertia is dominating the Coriolis term can usually be neglected. Surface waves is an example of the latter. The Rossby number is defined as

$$R_0 = \frac{U_0}{Lf_0} \tag{3.7}$$

where f_0 is the frequency of the motion. For small Rossby numbers, Coriolis forces dominate over inertia and is therefore important. With the effect of Coriolis, denoted as f, the boundary layer equations becomes (Myrhaug, 2012),

x-direction:

$$\frac{\partial u}{\partial t} + u\frac{\partial u}{\partial x} + v\frac{\partial u}{\partial y} + w\frac{\partial u}{\partial z} - fv = -\frac{1}{\rho}\frac{\partial p}{\partial x} + \nu\frac{\partial^2 u}{\partial z^2} \tag{3.8}$$

y-direction:

$$\frac{\partial v}{\partial t} + u\frac{\partial v}{\partial x} + v\frac{\partial v}{\partial y} + w\frac{\partial v}{\partial z} + fu = -\frac{1}{\rho}\frac{\partial p}{\partial y} + \nu\frac{\partial^2 v}{\partial z^2} \tag{3.9}$$

z-direction:

$$\frac{\partial p}{\partial z} = 0 \tag{3.10}$$

This means that there is no change in the pressure in z-direction through the boundary layer. This is an important assumption for solving the boundary layer equations, and the effect of this will be further elaborated on in Chapter 6.

Chapter 4

Wind and Current

The ocean surface is highly affected by the interaction with the atmosphere. Wind blowing over the ocean surface drives ocean currents and causes the development of ocean surface waves. In this Chapter, the long term effects of this interaction will be in focus i.e. the generation of wind-induced currents in the ocean surface. These ocean currents are the result of the interaction between wind drag, pressure gradients and the Coriolis force. These are referred to as the long term effects of the interaction between the ocean and the atmosphere, but there can be large deviations from the average currents, due to daily variations in weather and water-flow patterns (Pinet, 2016). Generation of wind, and how it interacts with the Coriolis force and the pressure forces in the atmosphere is important in order to understand the role of the wind in the atmosphere. The effect of wind in the ocean surface layers will also be described, as this is the mechanism behind the wind driven currents which transports large volumes of water in the ocean surface layers (Pinet, 2016).

4.1 Generation of Geostrophic Wind

Geostrophic balance describes the phenomenon in the atmosphere when there is a balance between the Coriolis forces and the pressure gradients forces (Myrhaug, 2006). Fluid moving between these areas of high and low pressure, creates the wind currents in the atmosphere (Pinet, 2016). Winds blowing high in the atmosphere where there is no effect of friction, are blowing along lines of constant pressures as a result of equlibrium between

the pressure gradient forces and the Coriolis force. According to Cushman-Roisin (1994) this implies that there is no pressure work performed on or by the fluid. These winds are called geostrophic winds, and are blowing at a height of approximately 1 km above the Earth's surface. (Myrhaug, 2006).

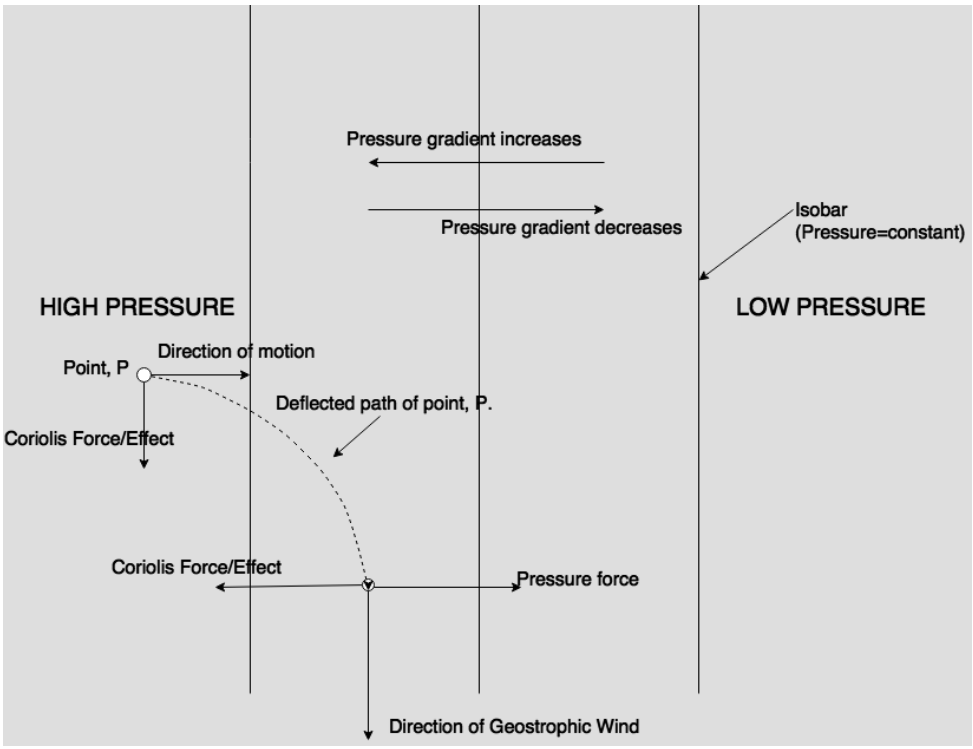

Figure 4.1: Generation of geostrophic winds. The figure is recreated from Myrhaug (2006).

Figure 4.1 shows the process of a fluid being deflected until the Coriolis force and pressure forces are in balance. When the air is moving from areas with high pressure to areas with low pressure, the wind will be influenced by the Coriolis force described in Section 2.2. In the Northern hemisphere, the Coriolis force will act normally to the right of the direction of motion, until a balance between the Coriolis force and the pressure forces occurs. The description in Figure 4.1 is simplified, with the isobars drawn as straight lines. In general, the isobars tends to have curvature, and this is taken into account as a centrifugal force. The result is that the wind moves in circles around the high and low pressure fields when the centrifugal force has obtained balance with the pressure force and the Coriolis force (Myrhaug, 2006).

4.2 The Ekman Layer

The Ekman Layer is an important phenomenon in order to explain how the mass transport in the ocean is affected by the wind and the Coriolis force. The Ekman Layer was first described by Vagn Walfrid Ekman in his doctoral thesis from 1902. Ekman was a student of Fridtjof Nansen, who during several travels to the arctic districts had observed that the ice bergs drifted, not in the direction of the wind, but at some angle of the wind. Nansen thought that this deviation in the drift angle could be due to the Earth's rotation, and Ekman got the task to investigate this mathematically. Ekman published the solution in Ekman (1905), today know as the Ekman layer solution. This solution has not only been important to understand the direction of the mass transport in the ocean, but it is also the foundation of Ekman pumping which generates the phenomenons of upwelling and downwelling in the oceans.

Due to horizontal stress from the wind on the ocean surface, the top layer of the ocean will move with the wind direction. As the ocean surface acts as a series of layers, this motion is transmitted due to friction from the surface layer and down in the water column. From each layer, energy is dissipated through internal friction, resulting in the wind only being able to penetrate a certain distance down in the water column. With the effect of the Coriolis force included, the wind-induced current will be rotated and continue to deviate from the direction of the wind further down in the water column. The interaction between the wind and the ocean surface creates a surface boundary layer, which is referred to as the surface Ekman layer (Grant, 2003). The deviation of the current direction continues down in the water column, as long as there is still energy that can be transported between the surface layers. Ekman (1905) found that for steady state conditions, a homogeneous fluid and geostrophic internal current given by $(u, v) = (u_g, v_g)$, the surface Ekman layer can be expressed as

$$u = u_g + \frac{\sqrt{2}}{\rho f d} e^{\frac{z}{d}} [\tau_x cos(\frac{z}{d} - \frac{\pi}{4}) - \tau_y sin(\frac{z}{d} - \frac{\pi}{4})] \tag{4.1}$$

$$v = v_g + \frac{\sqrt{2}}{\rho f d} e^{\frac{z}{d}} [\tau_x sin(\frac{z}{d} - \frac{\pi}{4}) - \tau_y cos(\frac{z}{d} - \frac{\pi}{4})] \tag{4.2}$$

where f is the Coriolis parameter, d is the depth of the Ekman layer and (τ_x,τ_y) is the shear force in (x, y)-direction, respectively. This solution showed that the surface current

was directed 45° to the right for the wind direction in the Northern hemisphere. The deviation of motion and decreasing velocity continues down through the water column, resulting in a picture that is often referred to as the Ekman spiral. The Ekman spiral (boundary layer) may penetrate to depths between 100 and 200 meters down in the ocean surface layer (Pinet, 2016).

The direction of the mass transport is the result of the average motion of the surface Ekman layer. The mass transport is therefore oriented 90° to the right of the direction of the wind stress (Cushman-Roisin, 1994), as seen in Figure 4.2. This is called the Ekman transport. The illustration in Figure 4.2 is based on Ekmans equations presented in Equation 4.1 and 4.2, and shows a theoretical value for the angle of the surface current. Observations have shown that this angle is smaller than what Ekman calculated (Cushman-Roisin, 1994).

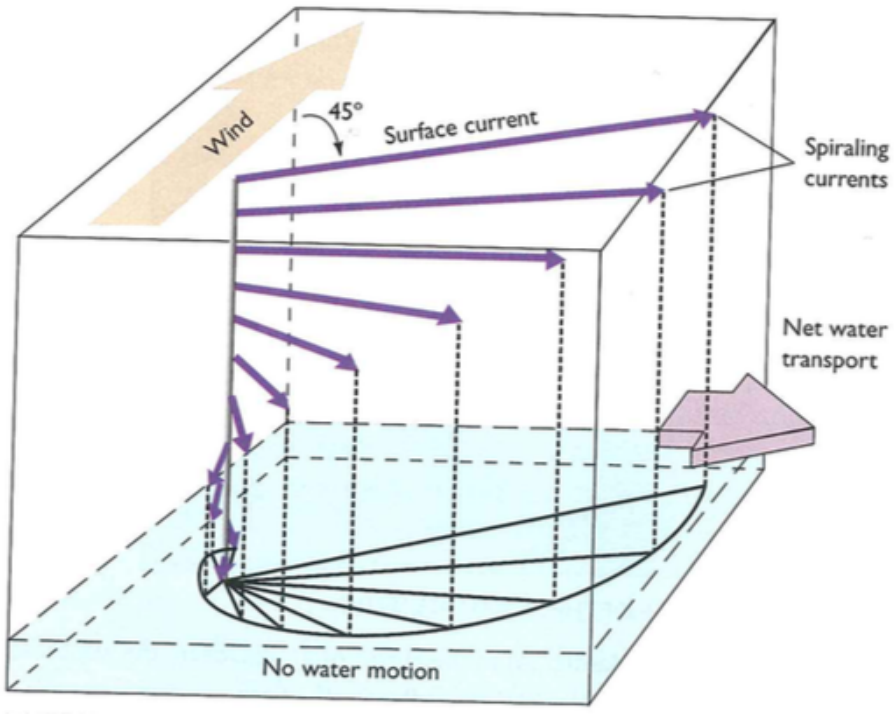

Figure 4.2: The deviation of the current direction in the Northern hemisphere, resulting in the Ekman Spiral. Figure from Pinet (2016).

The Ekman layer is not unique to the surface layer of the ocean, but can also be seen in i.e. the atmosphere. When the geostrophic winds blows over the Earths surface, they are exposed to frictional stress from the surface. This affects the geostrophic flow in

the same way as the ocean flow, rotating the wind direction and creating an Ekman spiral in the atmosphere. To balance the Ekman transport in the ocean, the atmospheric Ekman transport is directed to the left in the Northern hemisphere. The atmospheric mass transport is the same as the Ekman transport in the ocean, but due to major differences in density between water and air, the volume transport in the atmosphere is larger. The result is a boundary layer that reaches up approximately a kilometre in height (Cushman-Roisin, 1994; Grant, 2003).

4.2.1 Effects of Turbulence on the Ekman Layer

The statement in Section 4.2, claiming that the total mass transport in the ocean is directed 90° to the right of the direction of the wind, is only valid for a laminar flow. This solution of the Ekman equations is highly idealized, and according to Cushman-Roisin (1994), this can not be expected to match closely with the actual atmospheric and oceanic observations.

The high Reynolds number of geophysical flows shows that the flow is in a state of turbulence, and this is not accounted for in the original Ekman solution. This implies that the flow is characterized by irregularity, rapid mixing and increased rates of momentum, heat and mass transfer (Tennekes and Lumley, 1972). Without an exact theory of turbulence, several models are suggested, with varying results (Cushman-Roisin, 1994). However, two results seem to stand out in different models and field observations. The first is that the angle between the wind direction and the spiralling current, as shown in Figure 4.2, seems to be much smaller than 45° as found by Ekman (1905). Using different turbulence models to include the effects of a turbulent flow in combination with physical observations, this angle is found to range between 5° and 20°(Cushman-Roisin, 1994). The second result that seems to deviate from the surface Ekman layer solution is the effect of turbulence on the Ekman-layer thickness, i.e. the Ekman layer depth scale, d. In addition to these deviations, it is also pointed out by Cushman-Roisin (1994) that the Ekman Layer solution does not take the change of density between different layers in the ocean into account, resulting in stratification that will reduce the thickness of the Ekman layer.

4.3 Ekman Pumping

There is a clear connection between Ekman transport and how the wind drives subsurface currents. Consider a wind blowing parallel to a coastline in the Northern hemisphere. If the land is directed at the right of the direction of the wind, the Ekman transport will drive the water masses towards the shore, creating a downwelling i.e. warm, surface water is pressured down in the water column. Equivalent, if the wind is blowing in the opposite direction and the Ekman transport is directed away from the shore, this transport result in colder water from down in the water column to drive up. Hence, the phenomenons of downwelling and upwelling is important to ensure mixing in the ocean layers (Pinet, 2016).

Up - and downwelling is not limited to coastal areas. The variation of wind speed and direction at open waters will result in Ekman transports from different areas with different direction. Two opposing Ekman transports will produce convergence, with a doming of the water surface before the result is downwelling and sinking water (Grant, 2003). This is shown in Figure 4.3. In areas where water is transported away by the Ekman transport, there will be a divergence, resulting in upwelling. This vertical transport in the ocean is known as Ekman pumping, and it can be shown mathematically that this velocity is connected to the horizontal wind stress (Mellor, 1996).

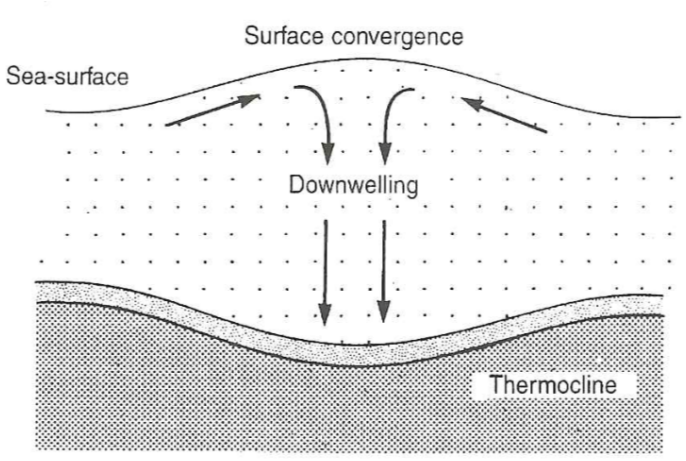

Figure 4.3: The figure shows how two opposing water transports results in convergence and downwelling. Figure from (Grant, 2003).

4.4 Inertial Motions

The inertial motions describe the inertial oscillations of a particle i.e. the trajectory of a particle only affected by the Coriolis force. Mellor (1996) demonstrates these effects by considering a barotropic, inviscid, low Rossby number flow. Implemented into the equations of motions, gives

$$\frac{\partial u}{\partial t} - fv = -g\frac{\partial \eta}{\partial x} \tag{4.3}$$

$$\frac{\partial v}{\partial t} + fu = -g\frac{\partial \eta}{\partial y} \tag{4.4}$$

Following the derivation in Myrhaug (2012), it is assumed that $\frac{\partial \eta}{\partial x}, \frac{\partial \eta}{\partial y}$ are constants and independent of x and y. Thus, u and v is also independent of x and y, and the right side of Equation 4.3 and 4.4 is equal to $-fv_g$ and fu_g, respectively. Here u_g and v_g describes a geostrophic flow. Solving Equation 4.3 and 4.4 for a water particle at the ocean surface, only effected by the Coriolis force and with initial velocity $u = u_0$ at time $t = 0$, shows that the particle moves in a circle with the radius of $r = \frac{u_0}{f}$. This is referred to as the inertial circle (Myrhaug, 2012). If u_g and v_g is unlike zero, this will be added to the inertial circle as a constant velocity assuming that frictional forces are neglected (Myrhaug, 2012). The motion of such a particle is shown in Figure 4.4.

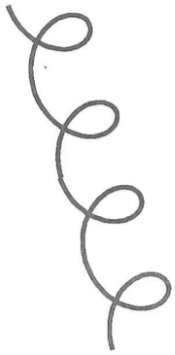

Figure 4.4: Trajectory of a particle with a constant velocity and rotating due to impact from the Coriolis force, only. Illustration from Mellor (1996).

Implementing the contribution from frictional forces will affect the inertial circle such that the radius will be reduced (Myrhaug, 2012). The effect of friction is also important in deducing the Ekman transport equations (Mellor, 1996). However, this solution is complicated, and will not be explained here.

Chapter 5

Turbulence Modelling

Turbulence modelling is a general term including different ways of taking into account the effect of turbulence in natural flows. A turbulent flow is difficult to describe precisely. The flow is characterized by randomness and irregularity, rapid mixing, dissipation, rotational and three-dimensional vorticity fluctuations. Due to the complexity and unpredictability of turbulence, there exists no theory completely describing the properties of a turbulent flow. Hence, turbulence modelling is necessary to predict the behaviour of a turbulent flow. A widely used approach is to separate the fluctuating property from its time-mean value (White, 2006) and deduce the Reynolds averaged equations. Then the momentum transfer can be described with an eddy viscosity, in an attempt to obtain a form of the equations that is similar to the laminar Navier-Stokes equations (Holmedal, 2002). This is the foundation for a turbulence model, and there are several models that can be applied depending on the problem that needs to be modelled. In this chapter the deduction of the Reynolds equations is shown before the concept of the generalized eddy viscosity is explained. Finally, a widely used turbulence model is presented.

5.1 The Reynolds Equations

The Reynolds equations can be found by applying time averaging to the basic equations of motions, resulting in both mean and fluctuating properties (White, 2006). Osborne

Reynolds first showed how this could be done by setting

$$u(x_i,t) = \overline{u(x_i,t)} + u'(x_i,t) \tag{5.1}$$

$$p(x_i,t) = \overline{p(x_i,t)} + p'(x_i,t) \tag{5.2}$$

where $\overline{u(x_i,t)}$ is the averaged velocity field and $u'(x_i,t)$ is the fluctuation. The same principle is applied for the pressure field, shown in Equation 5.2 (Holmedal, 2002). Substituting Equation 5.1 and 5.2 into Equation 3.5 (Continuity) and 3.6 (The Navier-Stokes equation) gives

$$\frac{\partial \overline{u_i}}{\partial x_i} + \frac{\partial {u_i}'}{\partial x_i} = 0 \tag{5.3}$$

$$\frac{\partial \overline{u_i}}{\partial t} + \frac{\partial u_i'}{\partial t} + \frac{\partial \overline{u_i u_j}}{\partial x_j} + \frac{\partial \overline{u_i} {u_j}'}{\partial x_j} + \frac{\partial {u_i}' \overline{u_j}}{\partial x_j} + \frac{\partial {u_i}' {u_j}'}{\partial x_j} = -\frac{1}{\rho}\frac{\partial \overline{p}}{\partial x_i} - \frac{1}{\rho}\frac{\partial p'}{\partial x_i} + \nu \frac{\partial^2 \overline{u_i}}{\partial x_j \partial x_j} + \nu \frac{\partial^2 {u_i}'}{\partial x_j \partial x_j} \tag{5.4}$$

By taking the average of the equations and utilizing that the mean of a fluctuation is zero, and that the mean of a mean value equals the mean value, gives

$$\frac{\partial \overline{u_i}}{\partial x_i} = 0 \tag{5.5}$$

$$\frac{\partial \overline{u_i}}{\partial t} + \frac{\partial \overline{u_i u_j}}{\partial x_j} = -\frac{1}{\rho}\frac{\partial \overline{p}}{\partial x_i} + \nu \frac{\partial^2 \overline{u_i}}{\partial x_j \partial x_j} - \frac{\partial \overline{{u_i}' {u_j}'}}{\partial x_j} \tag{5.6}$$

The last term in Equation 5.6 is not zero and is referred to as Reynolds stresses or turbulent stresses. This term acts as a stress on the fluid, and must be modelled. Different ways of modelling this stress gives rise to different turbulence models (Holmedal, 2002).

5.2 Generalized Eddy Viscosity Concept

One way of modelling the turbulent stresses, is to describe the turbulent momentum transfer with an equivalent eddy viscosity. This is based on phenomenon that the momentum transfer of a fully turbulent flow, away from solid walls, is dominated by large eddies. These eddies causes rapid mixing, which results in the unpredictable and random flow of turbulence (Johansson, 2002). The concept of the eddy viscosity was presented already in the 1870's, by Joseph V. Boussinesq. He suggested that the turbulent stresses were proportional to the mean-velocity gradients, and that the turbulent momentum transfer

could be described by an eddy viscosity. This means that the eddy, or turbulent viscosity can be described as a product of the characteristic length and velocity scales of the large energetic eddies (Rodi, 1993). Obtaining a form of the averaged Reynolds equations that is identical to the laminar Navier Stokes equations, only with the eddy viscosity instead of the laminar viscosity (Holmedal, 2002) can be done by setting

$$-\overline{u_i{}'u_j{}'} = \nu_T(\frac{\partial \overline{u_i}}{\partial x_j} + \frac{\partial \overline{u_j}}{\partial x_i}) - \frac{2}{3}k\delta_{ij} \tag{5.7}$$

Here $\delta_i j$ is the Kronecker delta function, ν_T is the eddy viscosity and k is the turbulent kinetic energy, given as

$$k = \frac{1}{2}\overline{u_i{}'u_j{}'} \tag{5.8}$$

The eddy viscosity, ν_T, needs to be specified. Based on how this is done, the resulting turbulence model will be either a zero-equation model, a one-equation model or a two-equation model. For a zero-equation model, the eddy viscosity can be assumed as

$$\nu_T = l_m V_m \tag{5.9}$$

Here l_m is the length scale and V_m is the velocity scale of the largest turbulent eddies in the flow. The first model to describe the eddy viscosity is known as the mixing length model, and the velocity scale V_m is here set to be proportional to $l_m \frac{\partial \overline{u}}{\partial z}$. Inserted in Equation 5.9, the eddy viscosity can be written

$$\nu_T = l_m^2 \left| \frac{\partial \overline{u}}{\partial z} \right| \tag{5.10}$$

The mixing length model is a zero-equation model based on the assumption that turbulent eddies interacts with each other similarly as molecules in a gas. This has later shown to be a poor assumption, and the mixing length model is therefore today taken to be inaccurate (Holmedal, 2002). To achieve a higher-order model, it is necessary to include a transport equation for the eddy viscosity, and this can be done by setting

$$\nu_T = c\sqrt{k} l_m \tag{5.11}$$

where k is the turbulent kinetic energy and c is a model constant. The velocity, V_m, is then assumed to be proportional to $\sqrt{k}$. A transport equation can be solved for the velocity k, and the result is a one-equation model where the diffusive and convective transport of the turbulent velocity is taken into account (Holmedal, 2002). For a two-equation model,

the diffusive and convective transport must be solved for both the turbulent length and velocity scales. According to Holmedal (2002), the most famous two-equation model is the $k-\epsilon$ model. An expression for the eddy viscosity, ν_T, is found from combining a modelling of the dissipation term, ϵ, and Equation 5.11 yielding

$$\nu_T = c_1 \frac{k^2}{\epsilon} \tag{5.12}$$

This approach has turned out to still be an important part of most of the turbulence models used today. Boussinesq's definition of the eddy viscosity is not a turbulence model in itself, it is merely a frame-work for constructing a turbulence model. How the different turbulence models chose to model the eddy viscosity determines the strength and application of the model (Rodi, 1993).

5.3 The $k-\epsilon$ Model

The $k-\epsilon$ model is a high-Reynolds number, two-equation model, which means that the diffusive and convective transport is included both for the turbulent length and velocity scales (Holmedal, 2002). Based on the $k-\epsilon$ model, it is common to write the transport equations for turbulent kinetic energy, k, and the dissipation rate, ϵ, as

$$\frac{\partial k}{\partial t} + \overline{u_j}\frac{\partial k}{\partial x_j} = \frac{\partial}{\partial x_j}(\frac{\nu_T}{\sigma_k}\frac{\partial k}{\partial x_j}) + \nu_T(\frac{\partial \overline{u_i}}{\partial x_j} + \frac{\partial \overline{u_j}}{\partial x_j})\frac{\partial \overline{u_i}}{\partial x_j} - \epsilon \tag{5.13}$$

$$\frac{\partial \epsilon}{\partial t} + \overline{u_j}\frac{\partial \epsilon}{\partial x_j} = \frac{\partial}{\partial x_j}(\frac{\nu_T}{\sigma_\epsilon}\frac{\partial \epsilon}{\partial x_j}) + c_{\epsilon 1}\frac{\epsilon}{k}\nu_T(\frac{\partial \overline{u_i}}{\partial x_j} + \frac{\partial \overline{u_j}}{\partial x_i})\frac{\partial \overline{u_i}}{\partial x_j} - c_{\epsilon 2}\frac{\epsilon^2}{k}, \tag{5.14}$$

where $\sigma_k, \sigma_\epsilon, c_{\epsilon 1}, c_{\epsilon 2}$ are model constants. The $k-\epsilon$ model is based on the generalized eddy viscosity concept, utilizing an eddy viscosity modelled as shown in Equation 5.12. The $k-\epsilon$ model, with fixed constants, is widely used. It has especially given satisfactory results when applied to two-dimensional wall boundary layers, free shear flows and even three-dimensional wall-boundary layers. Depending on which problem the model is applied to, boundary conditions must be described to the model. For a solid wall boundary e.g. the sea bed, the no-slip condition is applied. The no-slip condition implies that all velocities, both mean and fluctuating, is equal to zero at the wall. However, the dissipation rate ϵ is finite at the solid boundary. This creates a problem for two reasons. First, when

the equations are integrated through the thin wall layer, it requires many grid points to achieve a sufficient resolution, due to steep gradients in the wall layer. This requires an expensive computational tool. Second, as viscous forces are very important in the thin wall layer, the $k-\epsilon$ model which is a high-Reynolds number model, is not suitable (Rodi, 1993). However, it can be shown that for very high Reynolds numbers, this wall layer is so thin that the inertial and pressure forces can be neglected compared to the friction forces. Consequently, the universal law of the wall can be used, and it is only necessary to compute the outer fully turbulent layer and the wall shear stress (Schlichting and Gersten, 2000).

5.3.1 Universal Law of the Wall

In almost all turbulent flows it exsist a viscous thin layer close to the boundary. According to Rodi (1993) this can be described by empirical laws connecting the wall conditions e.g. wall shear stress, with the layer just outside the sublayer. For shear stress this is referred to as the universal law of the wall, and can be written as

$$\frac{U_{res}}{U_\tau} = \frac{1}{\kappa} \ln y^+ E \tag{5.15}$$

where U_{res} is the resultant velocity parallel to the wall, U_τ is the resultant friction velocity, y^+ is a dimensionless wall distance, κ is the von Kárman constant, and E is a roughness parameter (Rodi, 1993). This equation has proved to be mostly accurate in the area where $30 < y^+ < 100$, where the Reynolds stresses are nearly constant. Closer to the wall, boundary conditions have to be specified for k and ϵ (Rodi, 1993). In the transition between the thin viscous sublayer and the outer flow, i.e when $y^+ \to \infty$, the total turbulent production is equal to the dissipation of energy. This layer is therefore referred to as the equilibrium layer (Schlichting and Gersten, 2000).

The logarithmic profile that make up the law of the wall, can also be re-written to be used as a mean wind velocity profile to connect the wind stress with the ocean surface (Myrhaug, 2006). It is then written as

$$\frac{\overline{U}(z)}{\overline{U_{10}}} = 2.5\sqrt{C_D} \ln \frac{z}{z_0} \tag{5.16}$$

where z_0 is the sea surface roughness height, $\overline{U_{10}}$ is the mean wind speed at 10 meter elevation and C_D is a sea surface drag coefficient.

Chapter 6

Model Formulation

In this chapter, a brief description of the model used for simulating the tidal flow and wind driven currents, will be given. The applied model is a one-dimensional boundary layer model developed by Lars Erik Holmedal for his doctoral thesis (Holmedal, 2002). The velocities are calculated at grid points on a vertical line from the seabed to the surface. The model is used by Holmedal and Myrhaug (2013), and the description of the model in this thesis, closely follows their model formulation in Holmedal and Myrhaug (2013). Some modifications is executed on the model in order to simulate the flow beneath an increasing wind stress.

6.1 Governing Equations

Assume a tidal flow over an infinitely long, flat bottom. The coordinates at the bottom are localized such that the x - axis is positive towards the east, y is positive towards the north and z denotes the vertical distance from the bottom. The model simulates the velocities in a coastal area, where the water depth is set to be 120 meters. When investigating tidal flows over shallow and intermediate water depths, the horizontal scale is much larger than the vertical scale. Thus, the boundary layer approximation is valid over the entire water column. Including the assumption of a horizontally uniform flow, the advective terms vanish, and the Reynolds-averaged equations for conservation of the mean momentum and mass become

$$\frac{\partial u}{\partial t} = -\frac{1}{\rho_w}\frac{\partial p}{\partial x} + \frac{\partial}{\partial z}(\nu_T \frac{\partial u}{\partial z}) + fv \tag{6.1}$$

$$\frac{\partial v}{\partial t} = -\frac{1}{\rho_w}\frac{\partial p}{\partial y} + \frac{\partial}{\partial z}(\nu_T \frac{\partial v}{\partial z}) - fu \tag{6.2}$$

where u and v are the horizontal velocity components, p is the pressure, ρ_w is the density of water, ν_T is the eddy viscosity and f is the Coriolis parameter. The eddy viscosity is given by

$$\nu_T = c_1 \frac{k^2}{\epsilon}$$

where k is the turbulent kinetic energy, ϵ is the dissipation rate and c_1 is a model constant with the value 0.09. The $k-\epsilon$ model is used to simulate the turbulent viscosity. Subjected to the boundary layer approximation, the transport equations are given by

$$\frac{\partial k}{\partial t} = \frac{\partial}{\partial z}(\frac{\nu_T}{\sigma_k}\frac{\partial k}{\partial z}) + \nu_T((\frac{\partial u}{\partial z})^2 + (\frac{\partial v}{\partial z})^2) - \epsilon \tag{6.3}$$

$$\frac{\partial \epsilon}{\partial t} = \frac{\partial}{\partial z}(\frac{\nu_T}{\sigma_\epsilon}\frac{\partial \epsilon}{\partial z}) + c_{\epsilon 1}\frac{\epsilon}{k}\nu_T((\frac{\partial u}{\partial z})^2 + (\frac{\partial v}{\partial z})^2) - c_{\epsilon 2}\frac{\epsilon^2}{k} \tag{6.4}$$

where $(c_{\epsilon 1}, c_{\epsilon 2}\sigma_k, \sigma_\epsilon)$ are model constants with standard values of (1.44, 1.92, 1.00, 1.30), respectively.

6.2 Boundary Conditions

6.2.1 At the Sea Bottom

At the sea bottom it is assumed that the no-slip condition applies, giving

$$u = 0 \qquad v = 0 \qquad \text{at} \qquad z = z_0 \tag{6.5}$$

where z_0 is the height of the sea bed roughness.

For the turbulence field near the sea bottom it is assumed a local equilibrium between production and dissipation which gives the following boundary conditions for the turbulent kinetic energy, k, and dissipation, ϵ

$$k = \nu_T((\frac{\partial u}{\partial z})^2 + (\frac{\partial v}{\partial z})^2)^{\frac{1}{2}}/\sqrt{c_1}, \qquad \epsilon = (c1)^{\frac{3}{4}}\frac{k^{\frac{3}{2}}}{\kappa z_0} \tag{6.6}$$

evaluated at the first node from the bottom. Here $\kappa = 0.4$.

6.2.2 At the Surface

Since the steepness of the surface due to the tidal forcing alone is very small, it is assumed that the approximation of linear wave theory is valid. This leads to the boundary conditions at the surface being evaluated at the mean free surface, according to linear wave theory (Faltinsen, 1990; Holmedal and Myrhaug, 2013).

Pure tidally driven flows

For a pure tidally driven flow it is applied a condition of no shear at the ocean surface (mean free surface) giving

$$\frac{\partial u}{\partial z} = 0, \qquad \frac{\partial v}{\partial z} = 0 \tag{6.7}$$

where no shear is assumed at the mean free surface. It is assumed zero flux conditions, giving

$$\frac{\partial k}{\partial z} = 0, \qquad \frac{\partial \epsilon}{\partial z} = 0 \tag{6.8}$$

Pure wind driven flows and combined wind and tidally driven flows

A wind stress τ_s is included to simulate wind across the ocean surface. This is implemented directly into the momentum equations, giving $\nu_T \frac{\partial u}{\partial z} = \tau_s$ and $\nu_T \frac{\partial v}{\partial z} = 0$ for wind blowing from the West towards the East, at the free surface. The wind stress, τ_s is linked to the wind speed 10 meters above the sea surface through the relation $\tau_s = \rho_a c_d {U_{10}}^2$ where c_d is a friction factor and ρ_a is the density of air (Myrhaug, 2012; Holmedal and Myrhaug, 2013).

The velocity profile in the vicinity of the free surface is assumed to be logarithmic, hence:

$$k = \nu_T((\frac{\partial u}{\partial z})^2 + (\frac{\partial v}{\partial z})^2)^{\frac{1}{2}}/\sqrt{c_1}, \qquad \epsilon = (c_1)^{\frac{3}{4}} \frac{k^{\frac{3}{2}}}{\kappa z_s} \tag{6.9}$$

The turbulent kinetic energy k and the dissipation rate ϵ are evaluated at the computational node nearest the free surface. Here, z_s is a roughness at the ocean surface and it depends on the wave conditions. The value of z_s is discussed in Holmedal and Myrhaug (2013).

6.3 Forcing Function

For the tidal flow, the forcing is assumed to be in the East-West direction (i.e. along the x - axis). The tidal forcing is given by

$$-\frac{1}{\rho}\frac{\partial p}{\partial x} = -g\frac{\partial \zeta}{\partial x}cos(\sigma t) \tag{6.10}$$

where $\sigma = \frac{2\pi}{T_p}$, T_p is the tidal period and $\frac{\partial \zeta}{\partial x}$ is the amplitude of the mean ocean surface slope.

6.4 Numerical Method

To solve the Equations 6.1 - 6.4, a finite difference method is used, as explained in Holmedal and Myrhaug (2013). Geometric stretching of the mesh is applied such that there is a high resolution close to the sea bottom and close to the free surface where the flow is complex. In total 814 gridpoints were applied in the vertical direction.

The discretization in space resulted in a set of stiff differential equations for the horizontal velocity components, the turbulent kinetic energy and the dissipation rate. The equations were solved simultaneously in time by the integrator VODE (Brown, Byrne, and Hindmarsh, 1989b). A set of unique initial conditions are not applied since the solutions reaches steady state after a time interval of transients for any reasonable initial values (Holmedal and Myrhaug, 2013).

Chapter 7

Results and Discussion

In this chapter the results from the simulations are presented. Known physical theory from the theory background is used to discuss and validate the results. When referring to weak and strong wind, this corresponds to a shear stress at the ocean surface of $\tau_s = 0.2$ Pa and $\tau_s = 0.8$ Pa, respectively. This is equivalent to a wind speed of approximately 8 m/s and 16 m/s in the North sea. This can vary other places at the Earth as the friction factor c_d is depending on the atmospheric conditions (Holmedal and Myrhaug, 2013).

First, the simulations of a pure wind driven flow will be presented. The flow beneath a constant wind are validated by comparing the results to known theory and other studies where the flow driven by a constant wind has been investigated. Second, the simulations of a flow beneath an suddenly increasing wind are discussed with focus on the start-up of the wind. A selection of simulations of a pure tidally driven flow are also presented. Finally the results from a combined tidal and wind driven flow are presented and discussed.

7.1 Previous Work

The same one-dimensional boundary layer model was used in a project work written in preparation to the present work. The horizontal velocities u, v were calculated at grid points along the water column, with the highest resolution close to the sea bottom. The results were compared with field measurements conducted by King, Davies, and Soulsby (1985) and with the work conducted by Holmedal and Myrhaug (2013), who used the

same boundary layer model to predict the tidal flow. The result from the project work is presented in Appendix B, and therefore a smaller selection of simulations of a pure tidally driven flow are conducted for the present thesis.

7.2 Pure Wind Driven Flow

The following results are from simulations of a pure wind driven flow, with no tidal forcing. Here, the flow beneath a constant wind is simulated for 300 tidal periods with 180 000 and 200 000 outputs for weak and strong wind, respectively. The simulations revealed a large inertia of momentum in the system, which was especially clear close to the sea bottom for a flow beneath a weak wind. Therefore, a long simulation time was required to ensure a fully developed flow and to obtain steady state conditions. To avoid initial effects in the results, only two tidal periods are presented. The flow beneath an increasing wind is simulated for two tidal periods, where the wind is increasing linearly from the initial value equal to $\tau_s = 10^{-6} \approx 0$, to full wind speed. It was necessary to start the simulation with a wind stress unlike zero in order to get the code to run. The applied wind stress in the start-up of the ramp is small and it should not have any significance for the results. The particle trajectories in a pure wind driven flow beneath a constant and increasing weak wind are presented in Figure 7.1, for different heights above the sea bottom and for the ocean surface. The corresponding trajectories for a flow beneath a constant and increasing strong wind, are shown in Figure 7.2. Here, the trajectories in the constant wind driven flow are represented by a solid line, and the trajectories in an increasing wind driven flow are given by a dashed line.

From Figures 7.1a (weak wind) and 7.2a (strong wind), observations shows that the surface current is rotated to the right, relative to the direction of the wind which is blowing towards the East, i.e in the positive x- direction. This is caused by the Coriolis effect, which is directed to the right of the direction of motion in the Northern hemisphere (Myrhaug, 2006). As mentioned in Section 7.2, the simulations for a constant wind driven flow ran for a longer amount of time to obtain steady state conditions. This is achieved when the trajectories follows a straight line (solid lines), as seen in Figure 7.1b (weak wind) and in Figure 7.2b (strong wind). These figures shows that the rotation of the

surface current propagates down in water column. Due to friction between the horizontal water layers, the Coriolis effect rotates each layer to the right, relative to the upper layer. This process continues down in the water column, as long as there is energy from the wind stress. The result is that the direction of the current is rotated in a spiral, known as the Ekman spiral (Ekman, 1905), and this is seen for the trajectories due to both an increasing wind (dashed lines) and a constant wind (solid lines) in Figure 7.1a and Figure 7.2a for weak and strong wind, respectively.

Comparing the trajectories in the flow beneath a weak and strong wind, there is a difference in how many degrees the Ekman spiral is rotated. The wind at the surface is blowing in the same direction for both weak and strong wind, yet Figure 7.1b and Figure 7.2b shows that the trajectories beneath a weak wind are rotated several more degrees relative to the surface current, compared with strong wind. Since the Coriolis force, F_C, is proportional to u, v while the shear stress is proportional on the velocity gradients $\frac{du}{dz}, \frac{dv}{dz}$ both the shear forces and the Coriolis force depends on the horizontal velocities in the ocean (Holmedal, 2002). It is assumed that when the wind speed is increased to a four-times higher wind speed for strong wind compared to weak wind over the same amount of time, the motion down in the ocean due to the shear stresses from the wind will be affected. Assuming that shear stresses in a flow beneath a strong wind will propagate faster down in the water column and induce higher velocity gradients close to the sea bottom, this will lead to the shear stresses having a larger impact on the flow, not allowing the Coriolis force to rotate the motion the same amount of degrees as for weak wind in Figure 7.1b.

This assumption is validated by the theory presented in Chapter 4, where Ekman (1905) found that the surface current would be directed 45° to the right of the wind direction in the Northern hemisphere. The effect of a turbulent flow was not included in this solution. When this effect is included, Cushman-Roisin (1994) suggested that the current would be rotated between 5° - 20° to the right relative of the direction of the wind. Comparing the results for weak and strong winds shows that the surface current is rotated less in a flow beneath a strong wind, compared to weak wind. This is assumed to be caused by a higher wind speed resulting in larger velocity in the fluid, which results in a higher Reynolds number and a more turbulent flow. For weak wind there will be a lower velocity and a lower Reynolds number, i.e. the surface current beneath a weak wind is closer to the laminar solution presented by Ekman (1905).

Figure 7.1a for weak wind and Figure 7.2a for strong wind shows a difference in rotation of the trajectories in the flow due to an increasing wind (dashed lines) with the trajectories due to a constant wind (solid lines). Observations shows that for trajectories close to the ocean surface, the trajectory beneath a constant wind is rotated further to the right, while at depths closer to the sea bottom, the trajectory beneath the increasing wind is rotated furthest to the right. This may be caused by the difference in the simulation time between the flows beneath a constant and increasing wind. The flow beneath a constant wind has reached steady state conditions, whereas for an increasing wind the flow starts from the initial values in the beginning of the simulation. The rotation of the trajectories due to an increasing wind implies that a battle exist between the Coriolis force and the shear forces when the velocity in the flow is small. This will be further discussed later in this section.

Ekman (1905) found that the velocity would decrease down in the water column due to friction between the horizontal layers of water. This is shown in Figure 7.1b for weak wind and Figure 7.2b for strong wind, as the trajectories due to both a constant and an increasing wind becomes shorter close to the sea bottom. There is also a clear difference in the length of the trajectories beneath the constant and increasing wind, both for weak wind in Figure 7.1 and for strong wind in Figure 7.2. As Ekman (1905) showed, there is an energy loss between layers down in the water column. Combined with an inertia of momentum being transferred downwards in the water column, it takes some time for the energy due to the wind stress to affect the motion close to the sea bottom. This explains why the trajectories in the flow beneath an increasing wind is shorter compared to constant wind. The simulation of the constant wind ran for a longer period of time, and has therefore obtained steady state conditions and a fully developed flow.

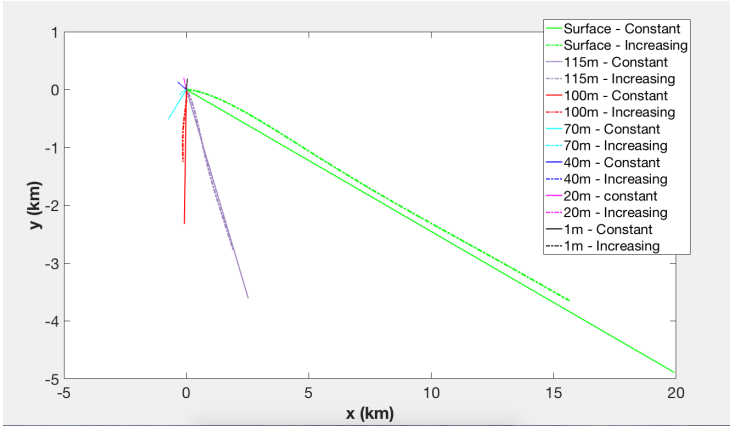

(a) Heights through the water column.

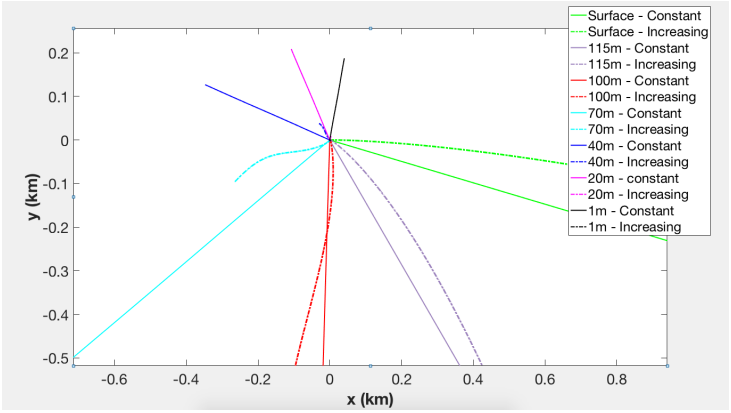

(b) Close-up of (a).

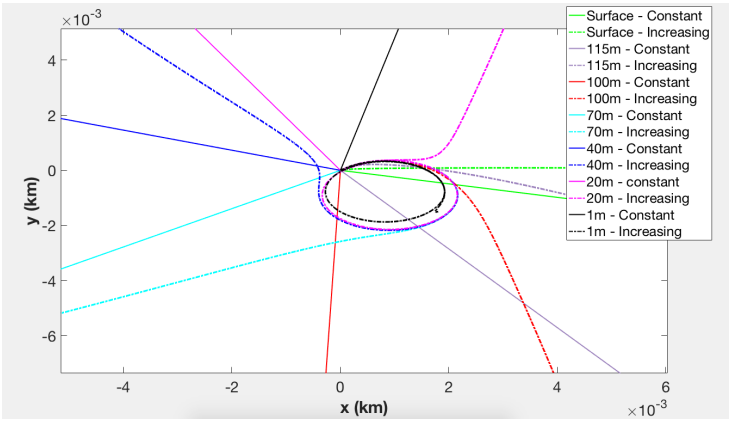

(c) Further close-up of (a), to see the near-bottom trajectories.

Figure 7.1: Particle trajectories at different heights above the sea bottom, beneath a constant and increasing weak wind. No tidal forcing.

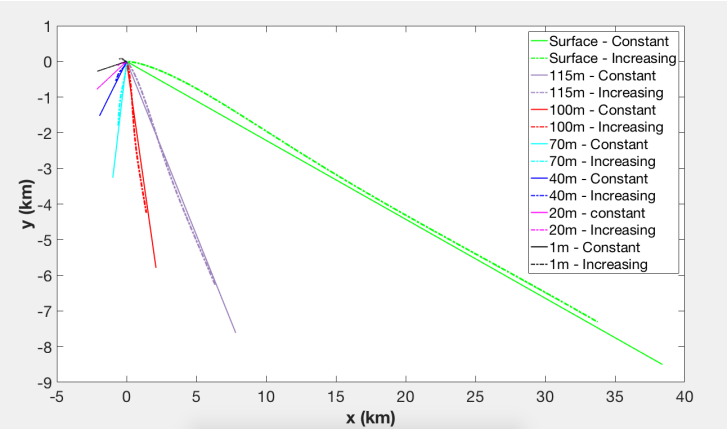

(a) Heights through the water column.

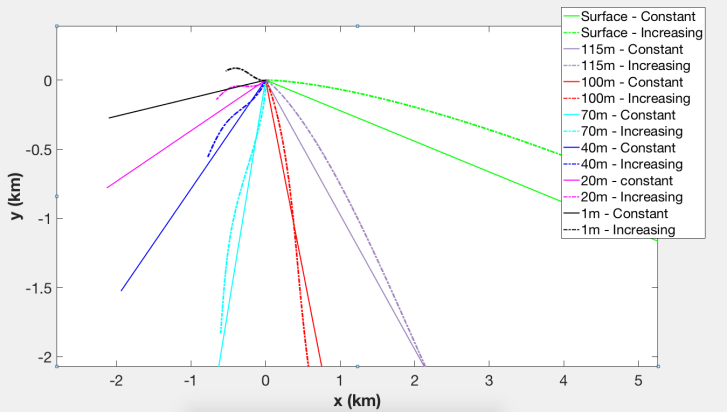

(b) Zoom.

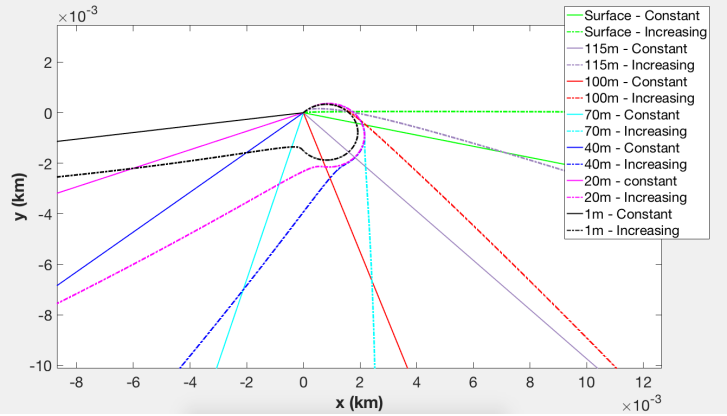

(c) Zoomed in to see the trajectories at the beginning of the simulation.

Figure 7.2: Particle trajectories at different heights above the sea bottom, beneath a constant and increasing strong wind. No tidal forcing.

Figure 7.3 shows the velocity profiles in a flow beneath a constant wind and the velocity profiles in a flow beneath an increasing wind after 2.45, 7.35, 12.25, 17.15 and 24.5 hours into the simulation. This is presented for both weak and strong winds, and shows that the strong wind affects the velocity in the ocean to a larger extent than the weak wind. The effect on the u-component is relatively large close to the surface, and this is consistent with the wind blowing in the u-direction. The effect of the wind in v-direction however, propagates further down in the water column for both strong and weak winds as seen in Figure 7.3b (weak wind) and 7.3d (strong wind). The velocity in v - direction corresponds with the rotation in the fluid, and in the beginning of the simulation of the flow beneath an increasing wind, there is little effects from rotation in the fluid compared with the flow beneath a constant wind. When the wind has blown for a longer time over the ocean surface, this allows the shear stress from the wind to penetrate the ocean surface layer to a larger extent than for a flow beneath a suddenly increasing wind. Shear stresses in the flow leads to turbulent mixing of the fluid and rotation (Brown et al., 1989a; Tennekes and Lumley, 1972), and the effect of this is seen for the velocity in v-direction in Figure 7.3b (weak wind) and Figure 7.3d (strong wind).

For a suddenly increasing wind driven flow, the trajectories moves in a circular motion at the beginning of the simulation when the wind is starting up. This is especially clear close to the sea bottom as seen in Figure 7.1c for weak wind and in Figure 7.2c for strong wind. To investigate this motion properly, the particle trajectories at different heights above the sea bottom are presented separately in Figure 7.4 for the flow beneath an increasing weak wind, and in Figure 7.5 for the flow beneath an increasing strong wind. Each figure is zoomed in at the trajectory in the starting point, and this results in some differences in the size at the axis. This is done in order to see the curvature of each trajectory at the starting point.

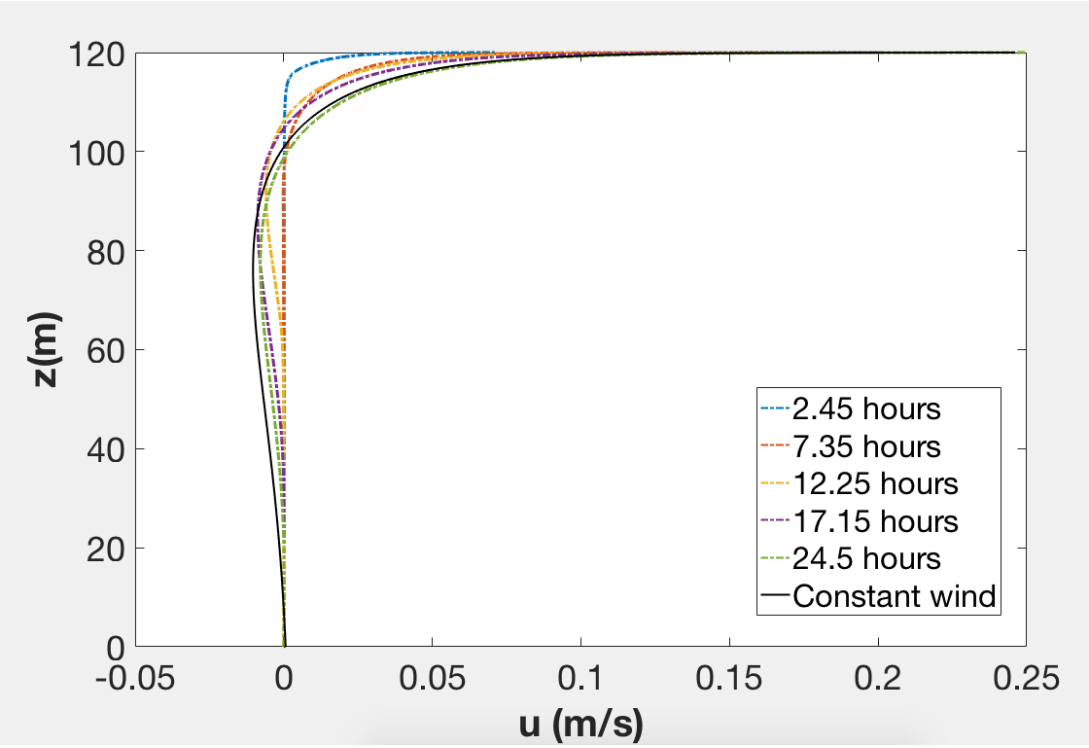

(a) Velocity in u - direction

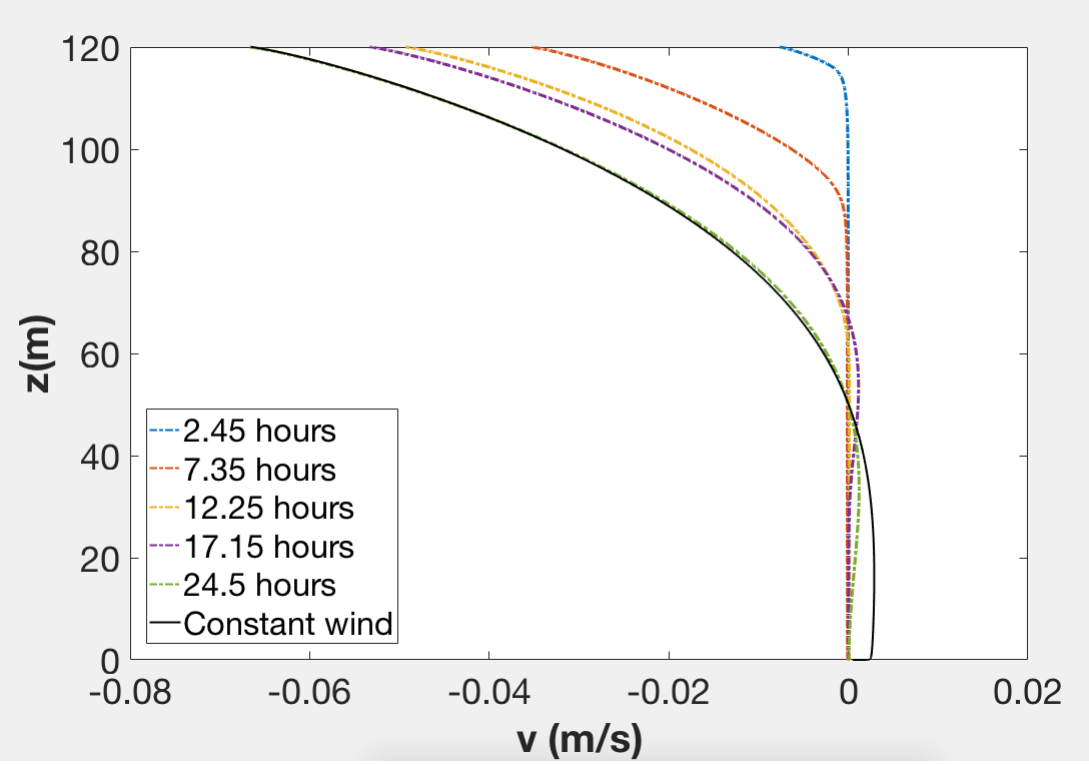

(b) Velocity in v - direction

Figure 7.3: Velocity profiles for a flow beneath an increasing and constant weak wind. No tidal forcing.

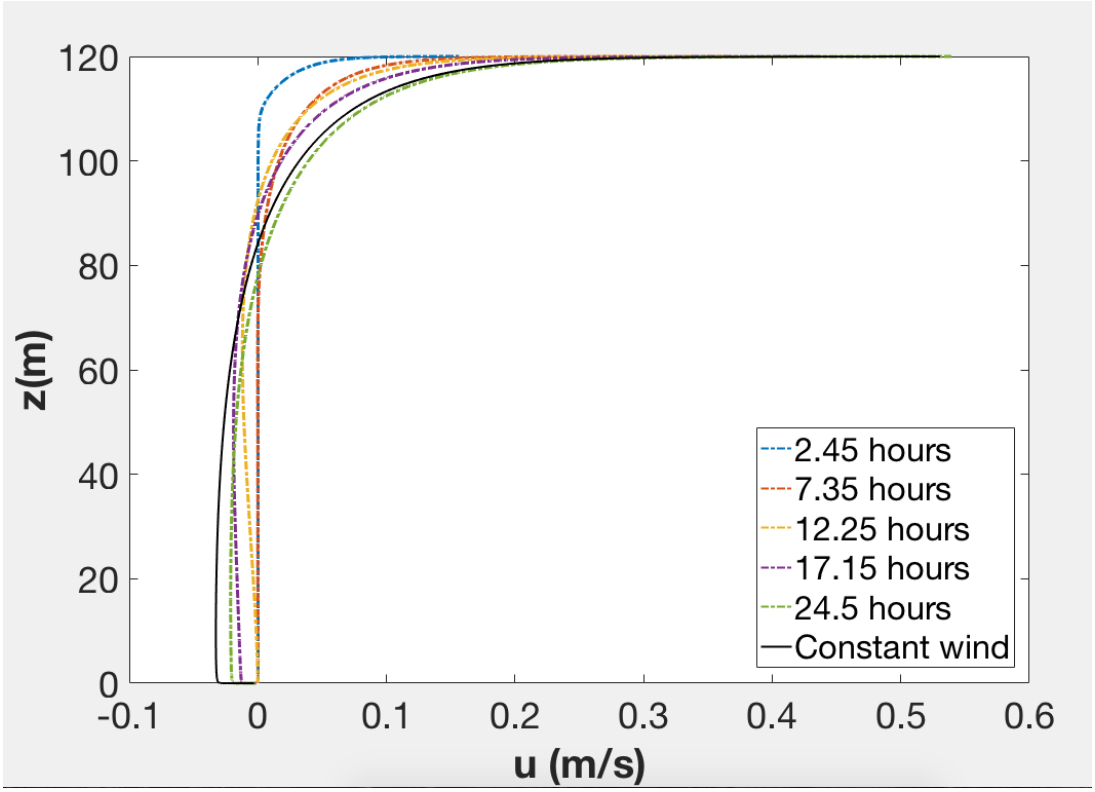

(c) Velocity in u - direction

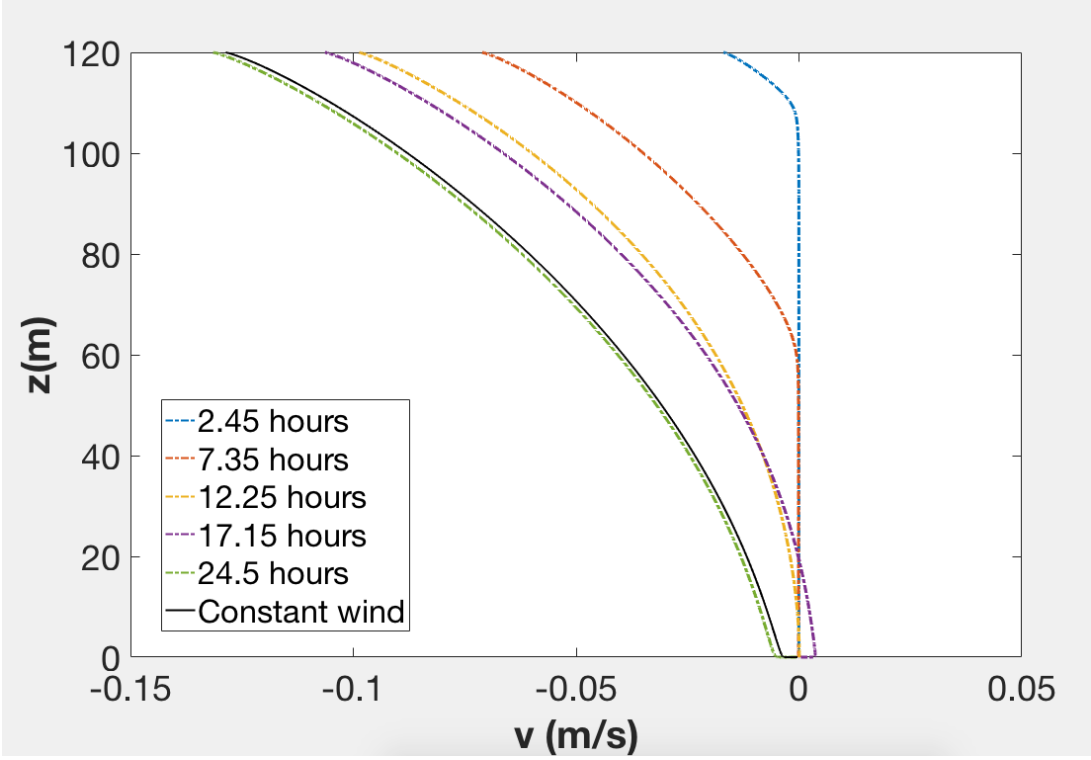

(d) Velocity in v - direction

Figure 7.3: Velocity profiles for a flow beneath an increasing and constant strong wind. No tidal forcing.

It appears that there exists some similarity between the trajectories close to the sea bottom and the inertial oscillations described in Chapter 4. The inertial oscillations are only influenced by the Coriolis force (Mellor, 1996) and it is therefore assumed that the Coriolis effect is the reason for the circular motion of the trajectories close to the sea bottom. The Coriolis effect is proportional to the horizontal velocity in the fluid, while the shear forces are depending on the velocity gradients in the fluid (Schlichting and Gersten, 2000; Holmedal, 2002). Because of the inertia down in the water column when the wind is blowing, the Coriolis effect dominates in the beginning, and rotates the trajectory before the shear stresses become large enough to affect the motion. This is consistent when comparing particle trajectories beneath weak increasing wind (solid line) with the strong increasing wind (dashed line) in Figure 7.6. For weak increasing wind at a certain depth, the trajectory follows a circular motion for a longer period of time compared with strong increasing wind at the same depth. This is e.g. seen in Figure 7.6d for 40 meters above the sea bottom. The ratio between the magnitude of the shear force F_τ and the Coriolis force F_C are shown in Figure 7.7 for different heights above the sea bottom, as a function of time. Figure 7.7a (weak wind) and Figure 7.7b (strong wind) shows that the Coriolis force is dominating in the beginning, for all heights except at the ocean surface. Further, as the wind speed at the ocean surface increases, the magnitude of the shear force becomes significant down in the water column. For heights close to the ocean surface, the Coriolis effect dominates for a shorter time period in Figure 7.7b for a strong increasing wind, compared to a weak increasing wind in Figure 7.7a. This is also consistent with what is seen for the particle trajectories for the flow in Figure 7.1 (weak wind) and Figure 7.2 (strong wind), where the trajectories in the flow beneath an increasing wind are rotated further to the right close to the bottom, compared with the trajectories in a constant wind driven flow which does not have this circular motion in the beginning of the simulation.

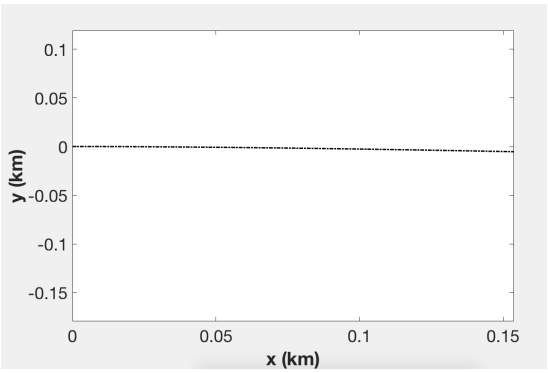

(a) At the ocean surface

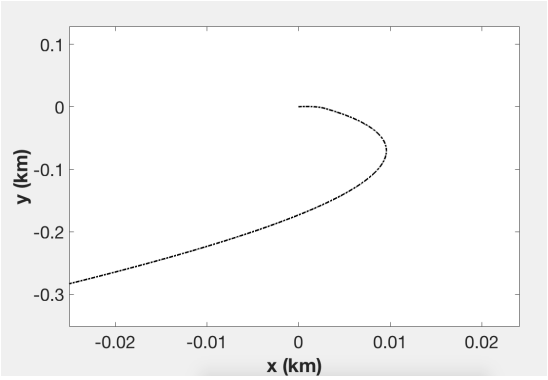

(b) 100 meters above the sea bottom

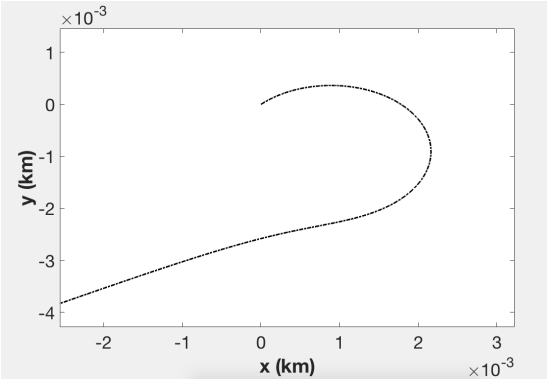

(c) 70 meters above the sea bottom

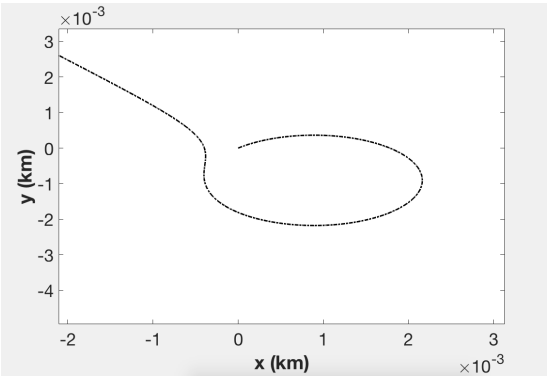

(d) 40 meters above the sea bottom

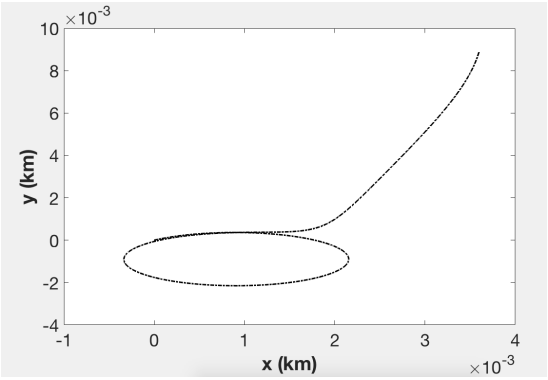

(e) 20 meters above the sea bottom.

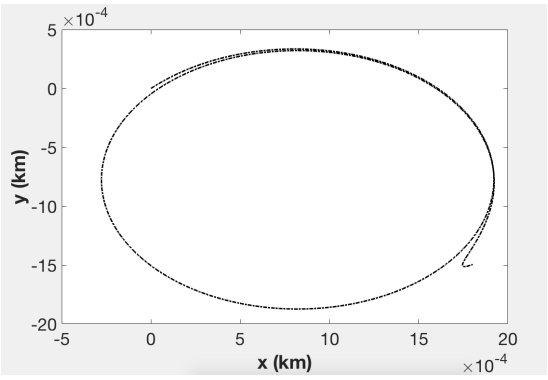

(f) 1 meter above the sea bottom

Figure 7.4: Particle trajectories beneath an increasing weak wind at different heights above the sea bottom. No tidal forcing. Close-up of the starting point.

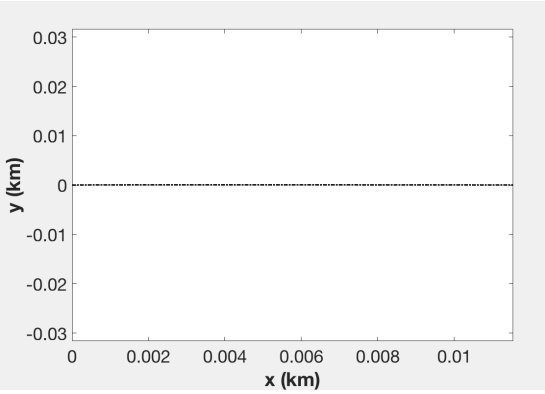

(a) At the ocean surface

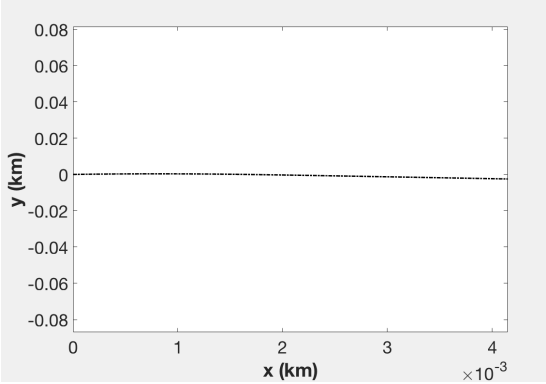

(b) 100 meters above the sea bottom

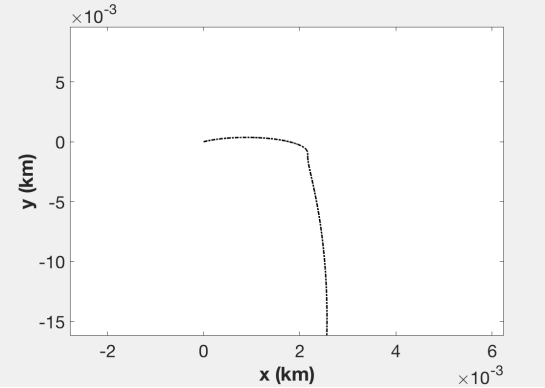

(c) 70 meters above the sea bottom

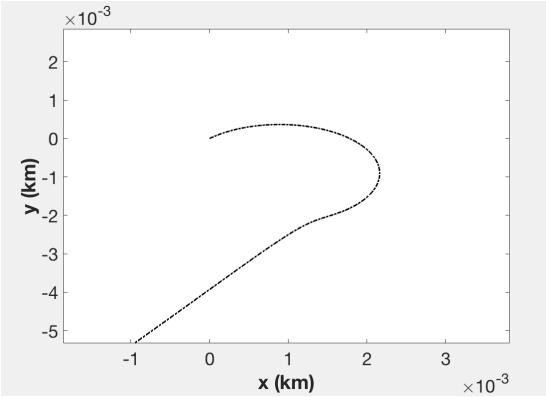

(d) 40 meters above the sea bottom

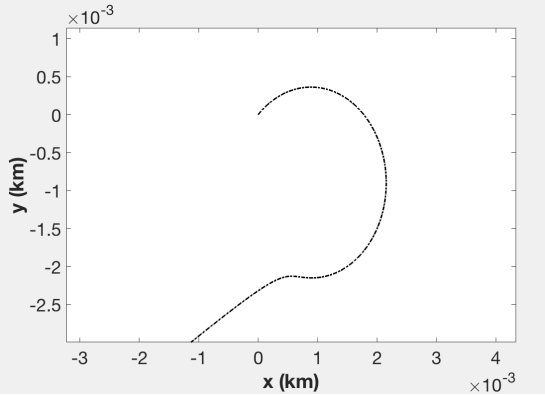

(e) 20 meters above the sea bottom

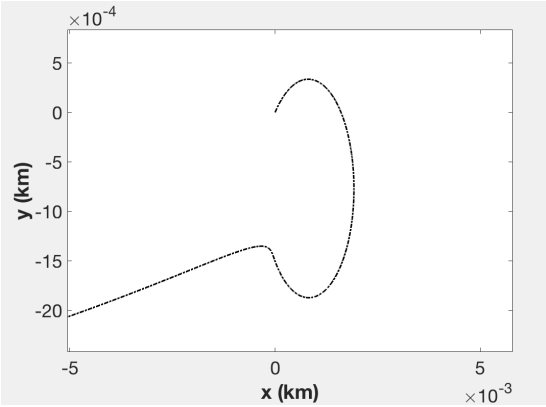

(f) 1 meter above the sea bottom

Figure 7.5: Particle trajectories beneath an increasing strong wind at different heights above the sea bottom. No tidal forcing. Close-up of the starting point.

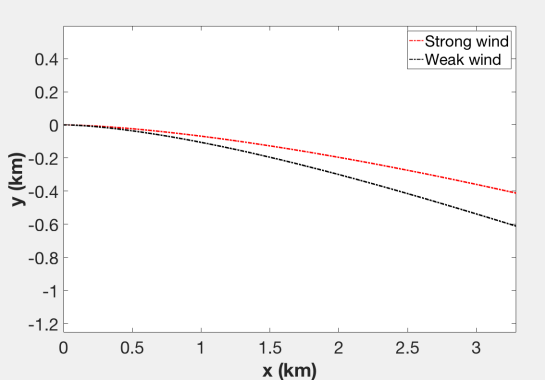

(a) At the ocean surface

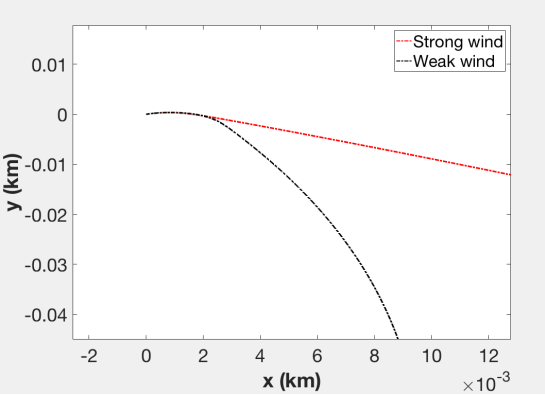

(b) 100 meters above the sea bottom

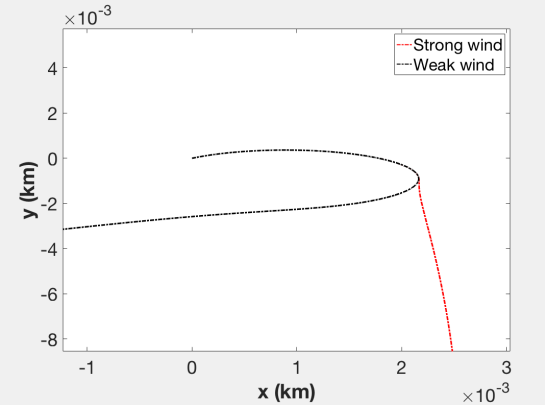

(c) 70 meters above the sea bottom

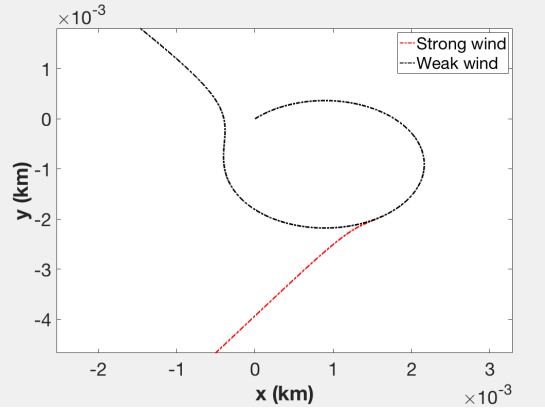

(d) 40 meters above the sea bottom

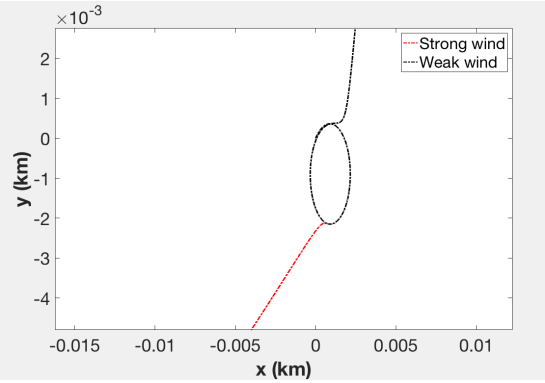

(e) 20 meters above the sea bottom

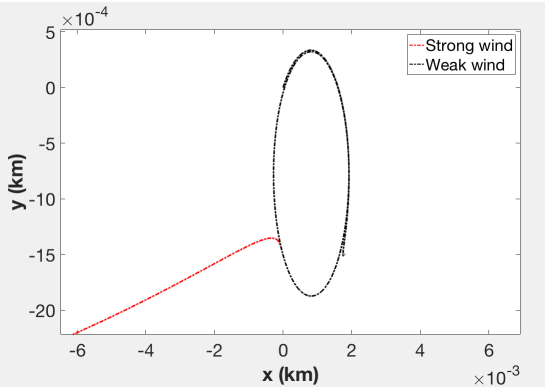

(f) 1.0 meters above the sea bottom

Figure 7.6: Particle trajectories beneath an increasing strong and weak wind at different heights above the sea bottom. No tidal forcing. Close-up at the starting point.

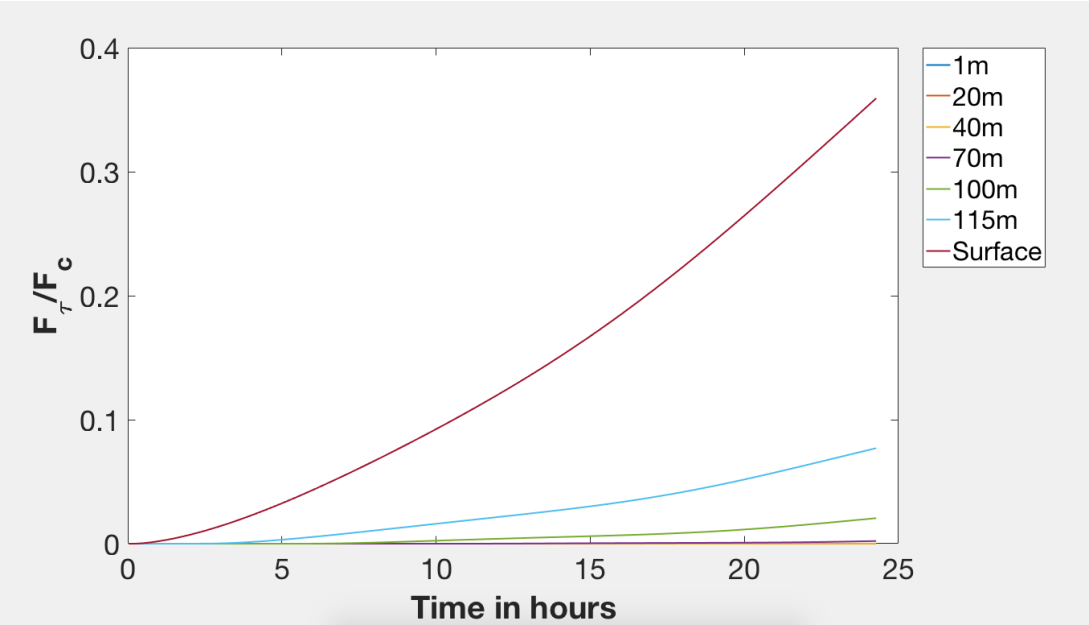

(a) Weak, increasing wind.

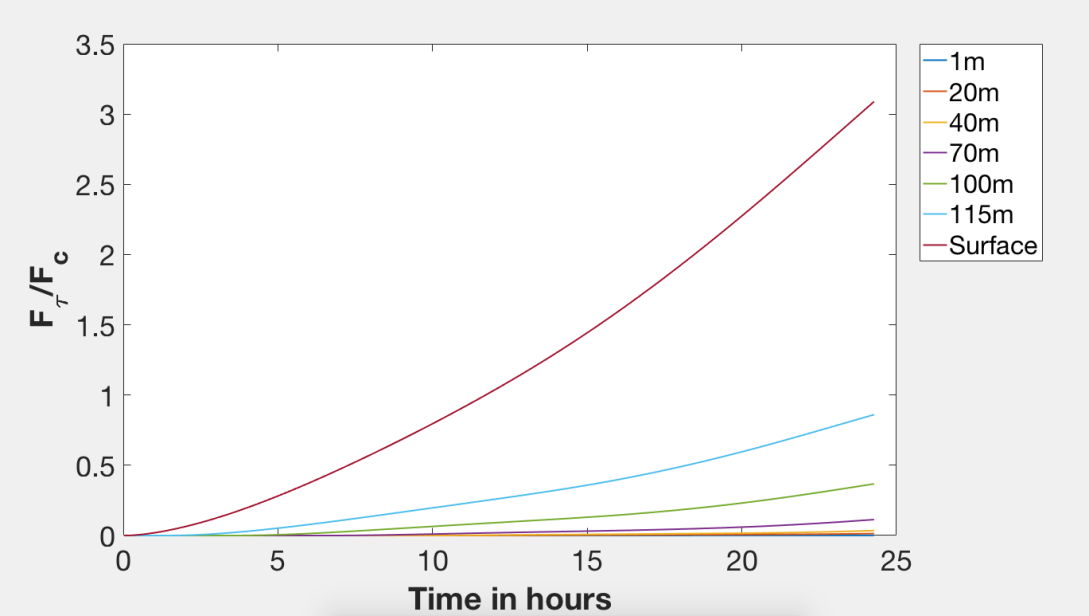

(b) Strong, increasing wind.

Figure 7.7: Shear force divided by Coriolis force for different heights above the sea bottom, as a function of time. No tidal forcing.

7.3 Pure Tidally Driven Flow

The pure tidally driven flow is simulated for 58 tidal periods, in order to obtain a fully developed flow field. Only the two final tidal periods are shown. In Figure 7.8 the velocity components in u- and v-direction during the two final tidal periods are presented. Close to the sea bottom there is an effect from the frictional drag due to the sea bottom roughness, as seen in Section 2.3 for a tidal velocity profile. The tidal wave penetrates the entire water column due to a very long wavelength, causing this vertical shear close to the sea bottom. This leads to turbulent mixing and it is necessary to utilize a turbulence model to solve the equations of motion (Holmedal, 2002; Brown et al., 1989a). Close to the surface there is no sign of shear stress on the velocities in Figure 7.8. The velocity profiles remain straight close to the sea surface which is consistent with no wind stress.

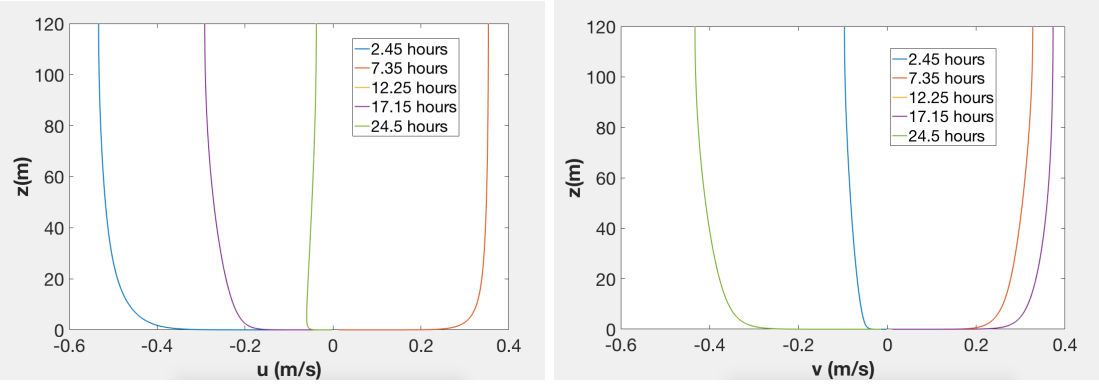

(a) In u - direction.

(b) In v - direction.

Figure 7.8: Velocity profiles in a pure tidally driven flow.

In Figure 7.9 the particle trajectory is shown at the ocean surface for a pure tidally driven flow. Since there is no effect of wind or waves, the trajectory is closed and Figure 7.9 shows how the water particles moves in an approximately elliptical path due to the Coriolis force influencing the tidal wave (Brown et al., 1989a). More results from a pure tidally driven flow are presented in Appendix B, where simulations of a pure tidally driven flow were compared with field measurements to validate the numerical model used in this thesis.

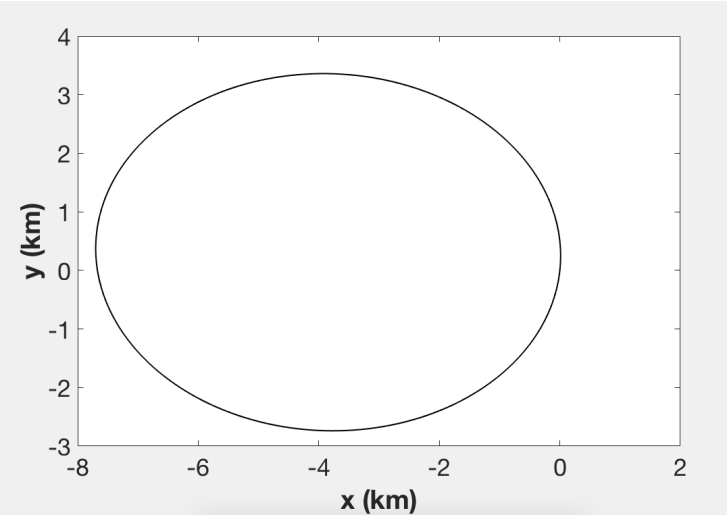

Figure 7.9: Particle trajectory at the ocean surface in a pure tidally driven flow.

7.4 Combined Tidal and Wind Driven Flow

The combined tidal and wind driven flow beneath a constant wind is similarly to the pure wind driven flow simulated for 300 tidal periods to obtain a fully developed flow. For weak and strong wind 180 000 and 200 000 outputs are applied, respectively. The result is presented for the two final tidal periods. For the flow beneath an increasing wind the tidal flow is first simulated for 58 tidal periods in order to ensure a fully developed tidal flow, before the wind is increased linearly from $\tau_s = 10^{-6}$ Pa to full wind speed during two tidal periods. Here, the model was set such that the boundary conditions at the ocean surface assuming no shear were applied in the beginning of the simulation, and then switched to a logarithmic profile when the wind stress was added. The boundary conditions are described in Section 6.2.2. The two final tidal periods are presented.

In Figure 7.10 the velocity profiles through two tidal cycles for a flow beneath a constant and an increasing, weak and strong winds are shown. The velocity component in u-direction is presented in Figure 7.10a (strong wind) and 7.10c (weak wind). The velocity in u-direction appears not to vary significantly over the water depth compared to a pure tidally driven flow, and this is likely caused by the tidal current dominating in the water column. There is a clear effect of an increased velocity in u-direction close to the surface layer however, and this is consistent with the wind blowing towards the East, i.e in positive x-direction.

The velocity in v-direction presented in Figure 7.10b (strong wind) and Figure 7.10d (weak wind) shows that the wind appears to have a larger effect on the velocity in v-direction compared with u-direction. The effect of a rough surface close to the sea bottom is seen for both the velocity components in u- and v-direction, and this is caused by the no slip condition at the sea bottom. This is the same for a flow beneath a strong and weak wind, with the single difference that the weak wind induces a slightly lower velocity in the flow. This difference between strong and weak wind is, however, minimal and this strengthens the assumption of a dominating tidal flow. Comparing the velocities in the flow in u - direction for both strong and weak wind with the velocities in v - direction, Figure 7.10 shows that the gradient is larger in u - direction, i.e. the effect of wind and tide is larger in u- direction. This corresponds with the tidal forcing being in East-West direction, i.e along the x-axis. This dominates the velocity in u-direction for the entire water depth, apart from close to the ocean surface where the effect of the wind is seen blowing towards the East. Comparing the velocity components at $t = 12.25$ hours in Figure 7.10 with the velocity profiles for a pure tidally driven flow in Figure 7.8 the difference is minimal.

Holmedal and Myrhaug (2013) did simulations of a flow beneath a strong constant wind with tidal forcing using the same numerical model which is applied here, and their results are consisting with what is presented in Figures 7.10a and Figure 7.10b. Comparing the results between a flow beneath a constant wind (solid line) with the flow beneath an increasing wind (dashed line), the difference is relatively small for the velocity in u-direction seen in Figure 7.10a (strong wind) and 7.10c (weak wind). The most significant difference is close to the surface at $t = 2.45$ hours into the tidal periods, and this is consisting with a very low wind speed for the increasing wind since it is started at $\tau \approx 0$ when $t = 0$. There is also a little difference after $t = 7.35$ hours, but after this the difference in u-direction is minimal. The effect of the wind is therefore most profound close to the ocean surface, and there seems to be little effect of the wind in the water column, i.e the tidal forcing is dominating in u-direction.

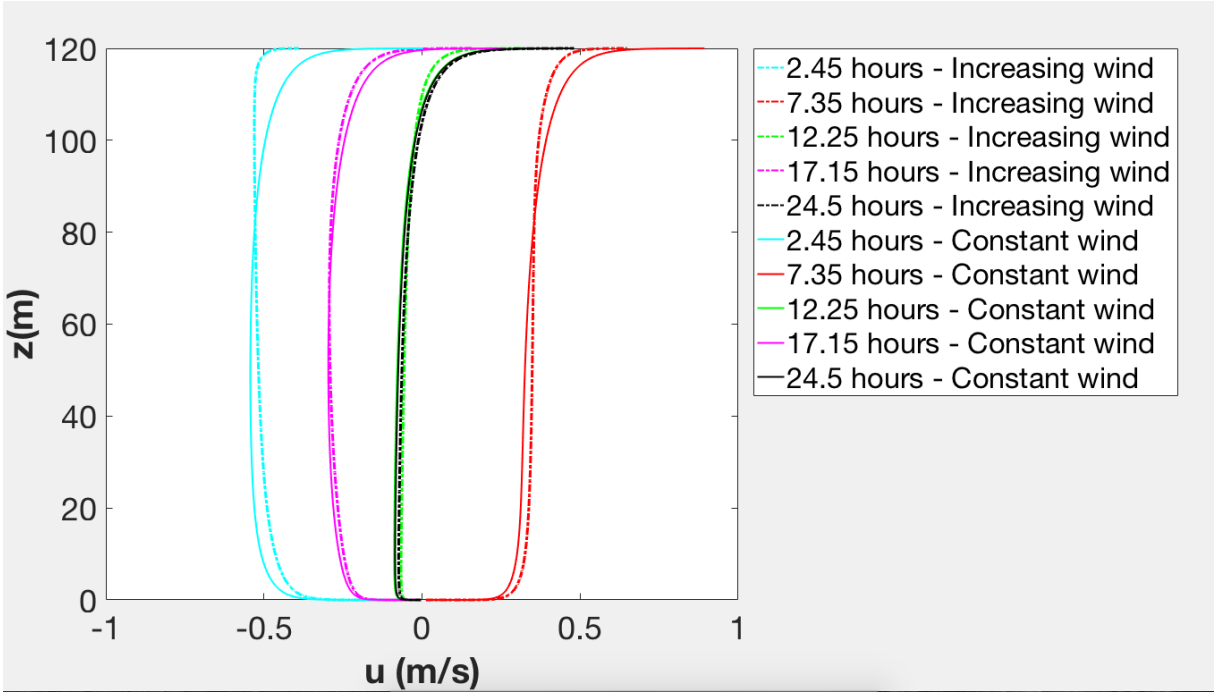

(a) Strong wind, u - direction.

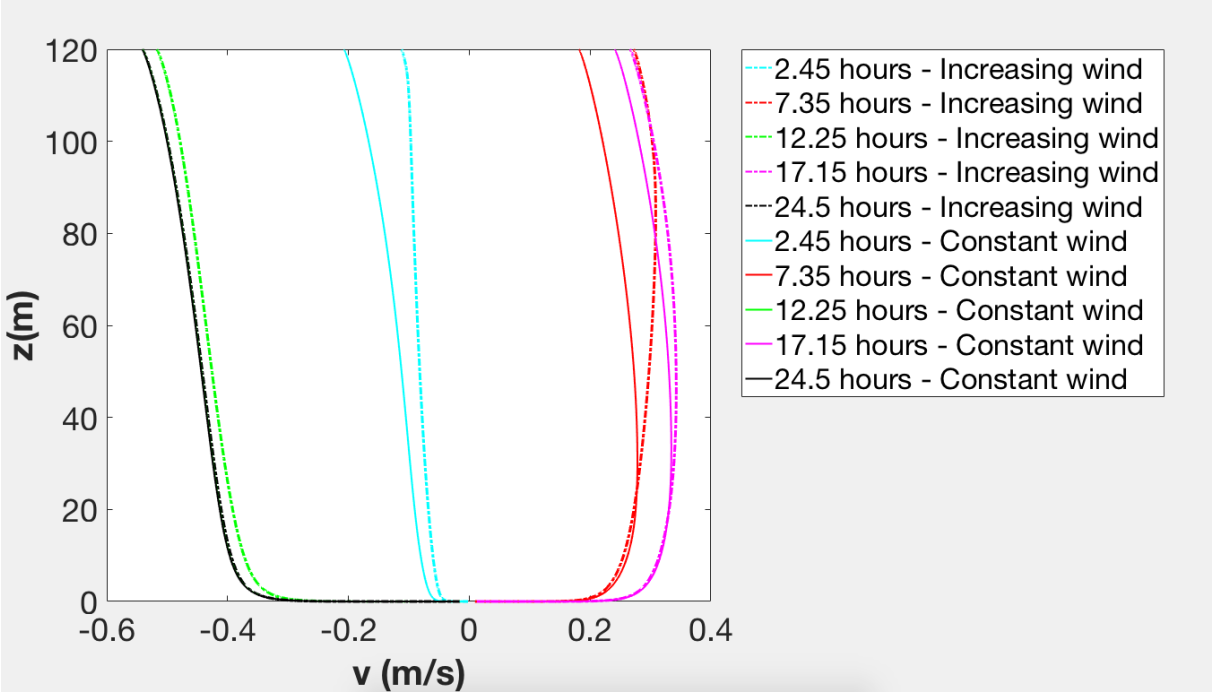

(b) Strong wind, v - direction.

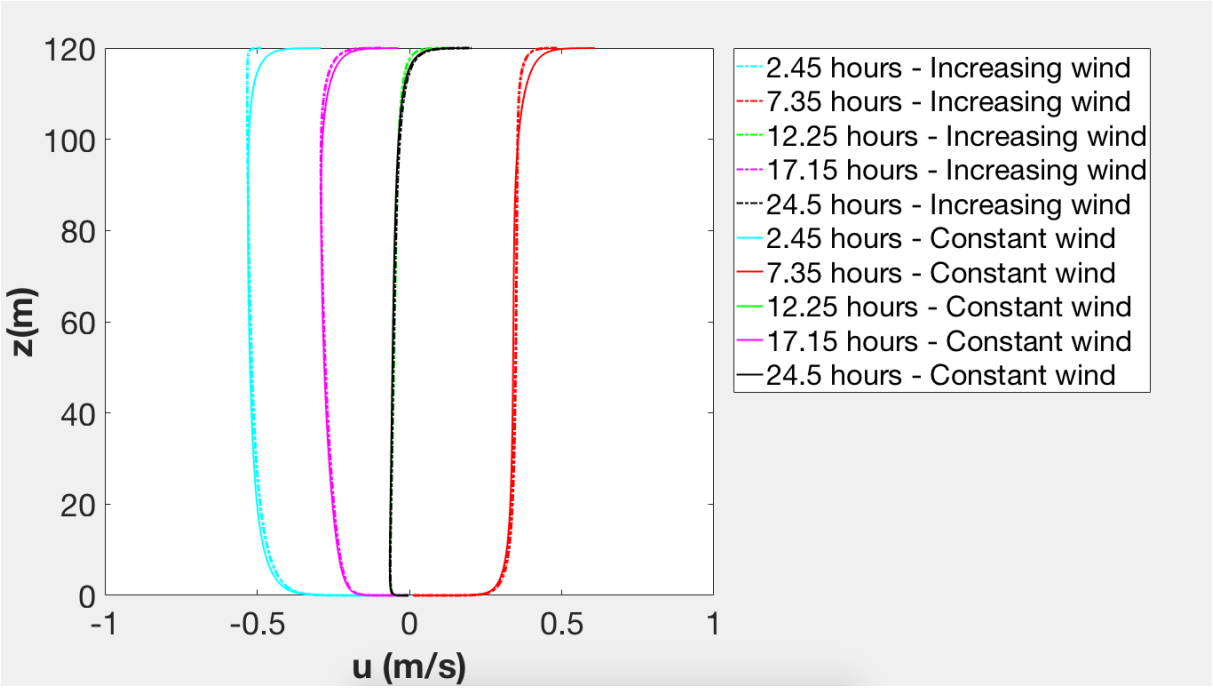

(c) Weak wind, u - direction.

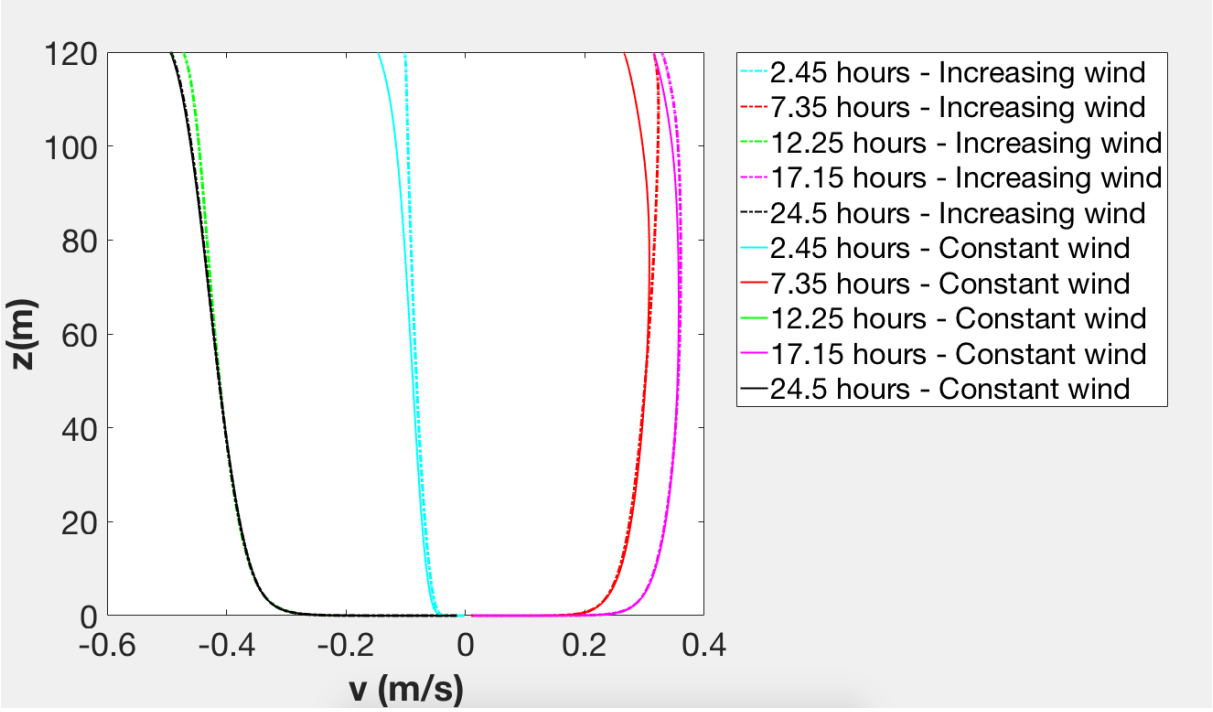

(d) Weak wind, v - direction

Figure 7.10: Velocity profiles beneath an increasing and constant, strong and weak wind. With tidal forcing

At e.g $t = 2.45$ hours into the cycle, Figure 7.10b reveals a clear difference between the velocity in v-direction of the flow beneath a constant and an increasing wind, and this deviation disappears at $t = 24.5$ hours when the wind speed for the two cases are the same. This shows that the wind does effect the horizontal velocity in the flow through the water column in v-direction. Compared with the velocity profile for a pure tidally driven flow, the gradient in v-direction is somewhat larger for a combined tidal and wind driven flow when the wind speed is high. For the flow beneath a weak wind the effect on the horizontal velocity in v-direction is minimal, and the tidal current is assumed to dominate.

The particle trajectories at different heights above the sea bottom in a constant and increasing wind driven flow is presented in Figure 7.11 and Figure 7.12 for strong and weak wind, respectively. The trajectories from the simulation of a flow beneath a constant wind are given by the solid line, while the red dashed line represents the trajectories for the flow beneath an increasing wind. Figure 7.11a (strong wind) and Figure 7.12a (weak wind) shows the trajectories at the ocean surface. The trajectory moves towards the right, which consists with the wind blowing in u - direction, i.e along the positive x- axis. Unlike the particle trajectory seen for the ocean surface of a pure wind driven flow in Section 7.2, the trajectories now moves in circles.

For a pure wind driven flow, Section 7.2 showed that beneath a constant wind the trajectory was represented by a straight line when the flow was fully developed, while the trajectory for a flow beneath a suddenly increasing wind varied to some extent. For a combined tidal and wind driven flow, the particle trajectories in Figure 7.11 and Figure 7.12 are moving in circles beneath both weak and strong winds. This elliptical motion is caused by the tides and the Coriolis effect, moving the ocean in a rotating wave as described in Chapter 2. Figure 7.11a shows the closed ellipse (blue line) due to a pure tidally driven flow, and how this elliptical motion of the flow obtains a drift caused by the winds (red and black line). At the ocean surface the effect of the wind is strong, compared to e.g at 100 meters above the sea bottom in Figure 7.11c, where the elliptical motion in the trajectory due to the tidal forcing is significant. For heights closer to the sea bottom in Figure 7.11f (1 meter above the sea bottom) the elliptical path due to the tidal forcing is dominating. When the wind stress is propagating down in the water column it loses energy due to friction between the horizontal layers of water. At a water depth

of 100 meters beneath the ocean surface the magnitude of the wind stress is reduced to approximately 4 % compared to the magnitude at the ocean surface (Myrhaug, 2012). The result is a minimal drift to the right due to wind stress close to the sea bottom, as seen in Figure 7.11f(strong wind) and Figure 7.12f(weak wind).

The same characteristics are seen for the particle trajectories of a flow beneath a weak wind in Figure 7.12. As expected, the effect of the weak wind blowing over the ocean surface is not penetrating as far down the water column as for strong wind in Figure 7.11. The elliptical path caused by the tidal forcing is more significant at the ocean surface in Figure 7.12a, with a drift to the right in the direction of the wind stress. Close to the sea bottom in Figure 7.12f there is very little effect of the wind stress and the trajectories are close to the closed elliptical path as seen for a pure tidally driven flow in Section 7.3.

Figure 7.11a (strong wind) and 7.12a (weak wind) shows that there is a large effect of the Coriolis force at the beginning of the simulation for a flow beneath an increasing wind, compared to a flow beneath a constant wind. The figures shows that the trajectories due to an increasing wind (red line) has a larger rotation and is being dragged less to the right due to the wind stress. The trajectories due to a constant wind (black line) is clearly being dragged to the right from the beginning of the simulation, especially for strong wind in Figure 7.11a. When the wind speed is low, the ratio between the shear force, F_τ, and the Coriolis force, F_C, is also assumed to be low. It appears that the Coriolis force is dominating over the shear force, and rotating the particle in circles before the shear force becomes large enough to move the trajectory towards the right, similarly as seen for the trajectories beneath a pure increasing wind driven flow. This is assumed to be affecting the trajectories in the beginning of the simulation of a flow beneath an increasing wind in Figure 7.12.

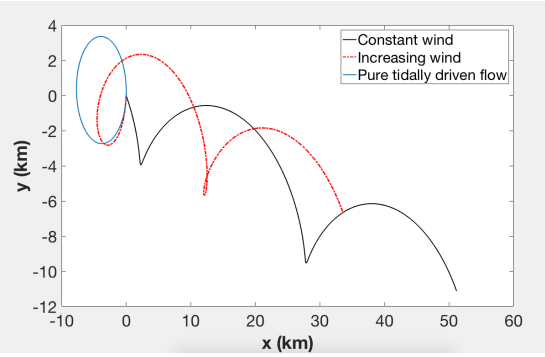

(a) At the ocean surface

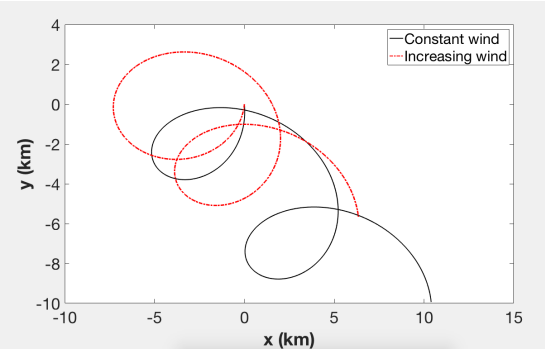

(b) 115 meters above the sea bottom

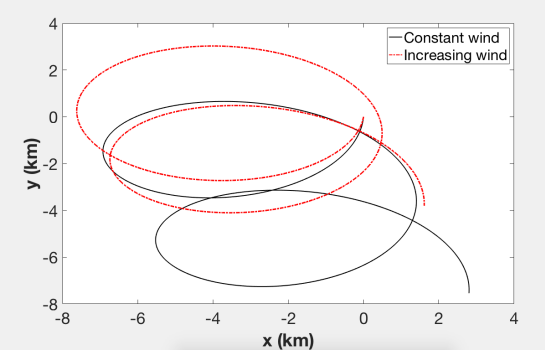

(c) 100 meters above the sea bottom

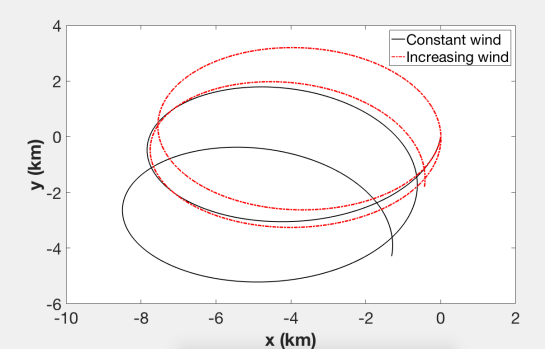

(d) 70 meters above the sea bottom

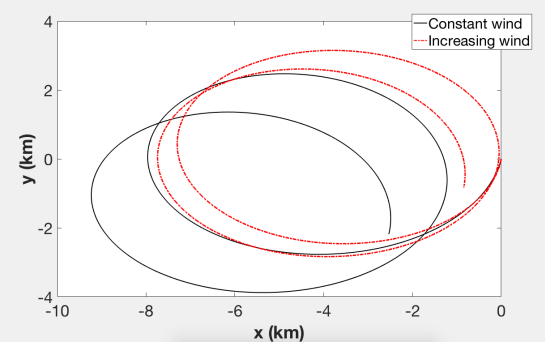

(e) 40 meters above the sea bottom

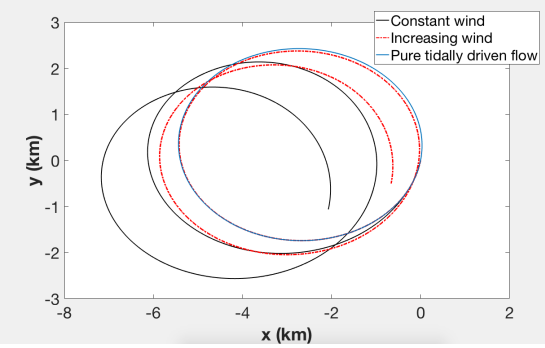

(f) 1.0 meters above the sea bottom

Figure 7.11: Particle trajectories at different depths above the sea bottom in a flow beneath a constant and increasing strong wind. With tidal forcing.

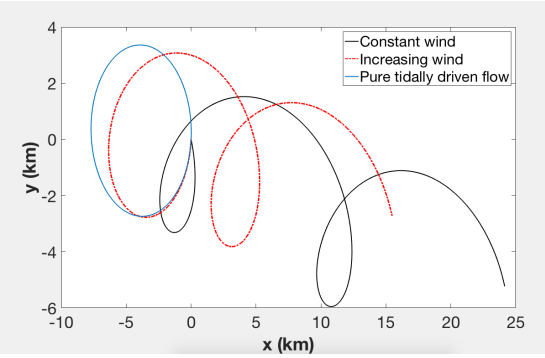

(a) At the ocean surface

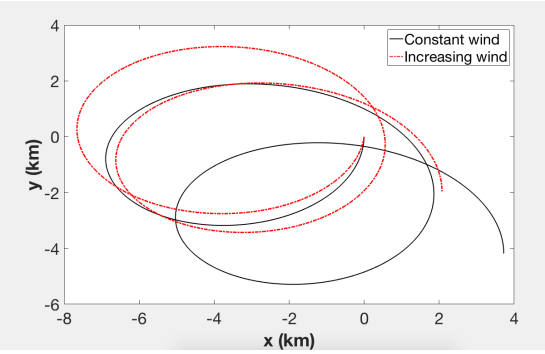

(b) 115 meters above the sea bottom

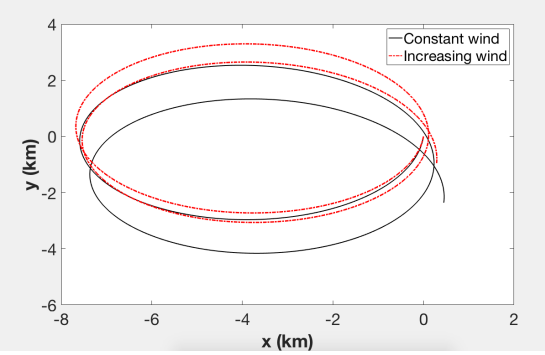

(c) 100 meters above the sea bottom

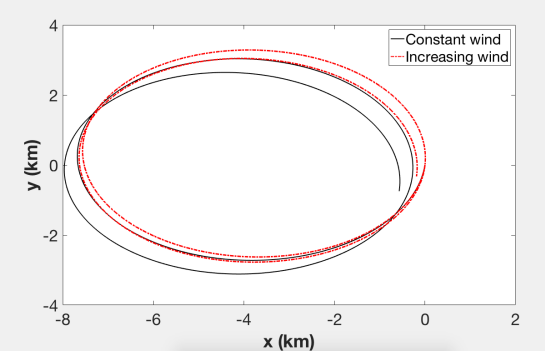

(d) 70 meters above the sea bottom

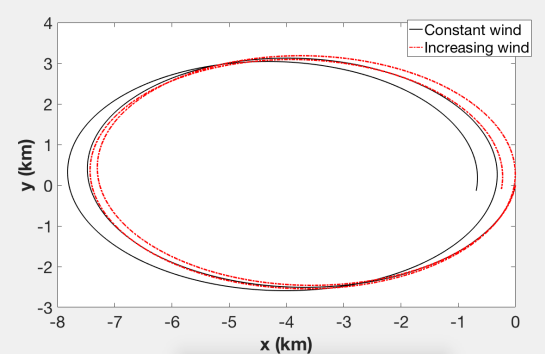

(e) 40 meters above the sea bottom

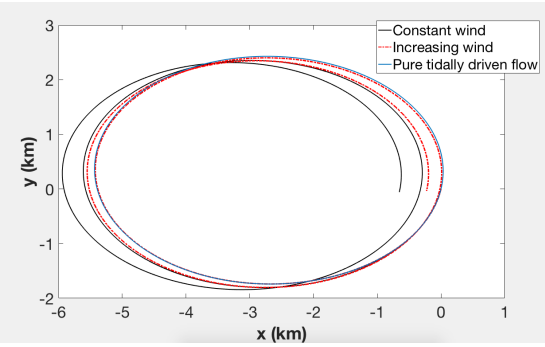

(f) 1.0 meters above the sea bottom

Figure 7.12: Particle trajectories at different depths above the sea bottom in a flow beneath a constant and increasing weak wind. With tidal forcing.

7.4.1 Mass Transport (drift)

The direction of the mass transport (drift) at the ocean surface and at 1 meter above the sea bottom for a combined tidal and wind driven flow is presented in Figure 7.13 for both a strong and weak wind. It is plotted by using the first and last coordinates of the particle trajectories in the flow. The vectors are not normalized, in order to see the difference in size, i.e. how far the drift is.

Comparing the drift at the ocean surface due to a strong wind in Figure 7.13a with the drift at the ocean surface due to a weak wind in Figure 7.13c, shows that there is a small difference between the direction of the drift when the wind is blowing in the positive x - direction. The most significant difference between strong and weak wind may be the distance of the drift in the flow. Figure 7.13a (strong wind) shows a drift approximately twice the distance in both x - and y - direction compared to Figure 7.13c (weak wind). The same difference is seen for the drift at 1 meter above the sea bottom. Figure 7.13b (strong wind) shows a drift twice as strong as in Figure 7.13d (weak wind). At 1 meter above the sea bottom it is seen in Figure 7.13b (strong wind) and Figure 7.13d(weak wind) that the drift is rotated to the right compared to the direction of motion. This is the effect of the Coriolis force and generation of the Ekman spiral as previously discussed.

There is a difference in the direction of the drift when comparing the flow beneath a constant and an increasing wind. The angle between the drifts seems to be larger at 1 meter above the sea bottom compared to the ocean surface. This may be caused by a larger difference between the magnitude of the wind stress. As previously mentioned, the magnitude of the wind stress is reduced to about 4% 100 meters down in the water column (Myrhaug, 2012), and the effect of the increasing wind will therefore be minimal down in the water column in the start-up of the simulation. There may also be an effect of inertia of momentum despite the presence of a tidal current. As mentioned in the beginning of Section 7.4, the simulation for a flow beneath a constant wind ran for 300 tidal periods with wind, in order to obtain a fully developed flow and there is therefore no inertia of momentum or unsteady flow affecting the direction of the drift beneath a constant wind. The deviation between the drift in the flow beneath a constant and increasing wind may be interesting when predicting mass transport at different heights over the water column, since the winds in e.g. the North sea is transient and can change direction and magnitude

suddenly. Since a fully developed flow requires steady conditions over several tidal periods these conditions are rare in natural environments, at best.

Comparing the flow beneath a strong wind at 1 meter above the sea bottom, Figure 7.13b shows that the drift due to a constant wind (orange line) is rotated further to the right relative to the direction of motion compared to the drift beneath an increasing wind (blue line). As mentioned, the rotation is the effect of the Coriolis force. For a pure wind driven flow in Section 7.2 the results showed that the particle trajectory close to the sea bottom beneath an increasing wind were rotated further to the right compared to the trajectory beneath a constant wind. It was assumed that this was caused by an inertia of momentum or the effects of an unsteady flow close to the sea bottom. The results in Figure 7.13b and Figure 7.13a shows that the trajectory beneath a constant wind is rotated furthest to the right, both at the ocean surface and the sea bottom. This is consistent with what was seen for the ocean surface of a pure wind driven flow. Here, the drift in a flow beneath a constant wind is rotated furthest to the right, also close to the sea bottom. This is likely to be an effect of the tidal current, resulting in vertical shear along the ocean surface and turbulent mixing in the flow (Brown et al., 1989a). This causes an increased shear force not allowing the Coriolis force to dominate for the same amount of time as in a pure wind driven flow, despite a low wind stress in the beginning of the simulation. The tidal current dominates the flow. This is also seen beneath a weak wind in Figure 7.13c (ocean surface) and in Figure 7.13d (1 meter above the sea bottom). The Coriolis force is assumed to have a larger resulting effect on the flow beneath a constant blowing wind since the horizontal velocities in the flow is larger. This results in the mass transport (drift) beneath a constant wind is rotated further to the right over the entire water column, compared to the mass transport (drift) beneath an increasing wind.

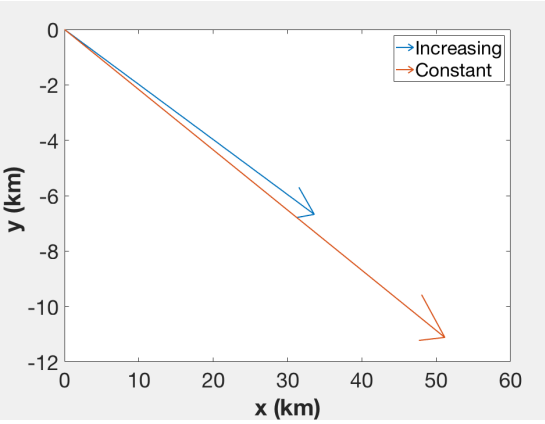

(a) Drift at the ocean surface in a flow beneath a strong wind.

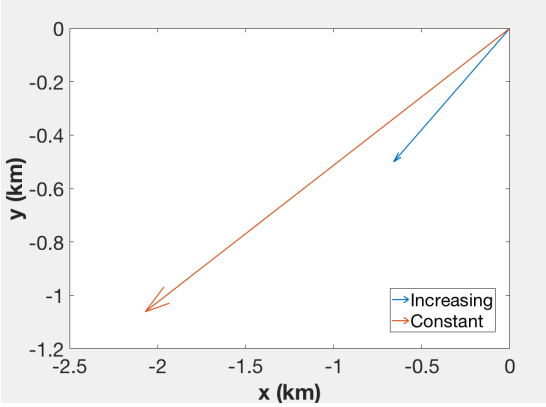

(b) Drift at 1 meter above the sea bottom in a flow beneath a strong wind.

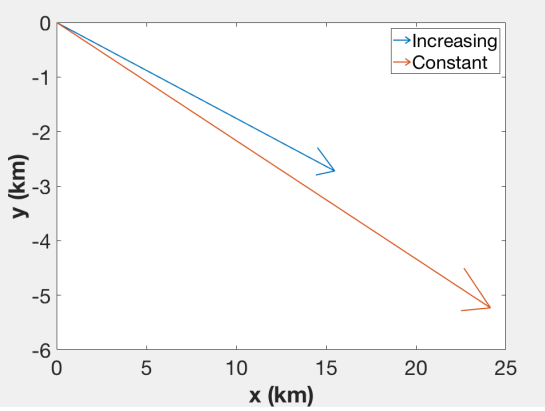

(c) Drift at the ocean surface in a flow beneath a weak wind.

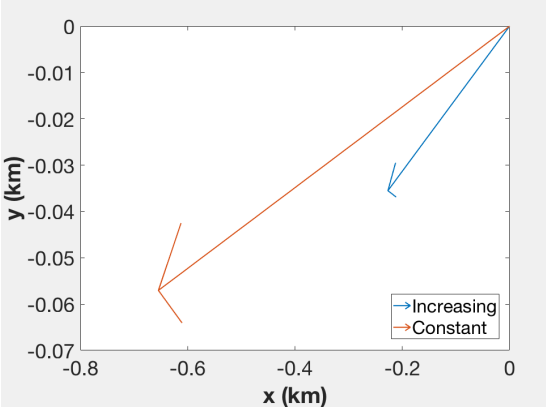

(d) Drift at 1 meter above the sea bottom in a flow beneath a weak wind.

Figure 7.13: Direction of mass transport (drift) in a combined tidal and wind driven flow. The drift is shown for a flow influenced by both a constant and increasing wind, respectively.

Chapter 8

Summary and Conclusion

The first objective of this thesis was to investigate the start-up of a pure wind driven flow. This is done by comparing the difference between a fully developed flow beneath a constant blowing wind and the flow beneath an increasing wind. In both cases there are no tidal forcing. The second part was to investigate the effect of a sudden wind imposed on a tidally driven flow. Here, an increasing wind is applied on a fully developed tidally driven flow, and compared with a fully developed tidal flow beneath a constant blowing wind. Studying the tidally driven flow beneath an suddenly increasing wind starting at zero wind stress have, to the authors knowledge, not been done before. For both a pure wind driven flow and a combined tidal and wind driven flow the difference between a strong and weak wind are included.

The results shows that there is a difference in how many degrees the Ekman spiral is rotated when comparing the pure wind driven flow beneath a strong and weak wind. The current close to the sea bottom beneath a weak wind is rotated further to the right relative to the direction of the wind at the ocean surface. This is assumed to be caused by a more turbulent flow due to strong wind, which according to Cushman-Roisin (1994) decreases the rotation of the surface current in the Ekman layer. This difference between the flows beneath strong and weak winds are consistent for both constant and increasing winds.

The particle trajectories in a flow beneath an increasing wind appears to move in a circular motion in the start-up of the simulation when the wind speed is low, especially at depths close to the sea bottom. This motion is similar to a trajectory only affected by the Coriolis

force. The Coriolis force is proportional to the horizontal velocities u, v, and the shear forces are proportional to the velocity gradients $\frac{du}{dz}, \frac{dv}{dz}$, and the results shows that the Coriolis force dominates over the shear stresses when the horizontal velocities are modest. This may be caused by an inertia of momentum down in the water column. This is validated by the velocity profiles for a pure wind driven flow showing that in the start-up of the wind, e.g after $t = 2.45$ hours the effect of the wind has the highest impact on the flow close to the ocean surface. This implies that both the horizontal velocities u, v and the velocity gradients $\frac{du}{dz}, \frac{dv}{dz}$ close to the sea bottom are small, resulting in the Coriolis force dominating over the shear forces.

For a combined tidal and wind driven flow, the velocity profiles shows that the tidal flow is dominating for the entire water column, resulting in little change in the velocity components in z-direction, except close to the ocean surface in the direction of the wind. A clear effect of the roughness close to the bottom is also seen, as expected (Brown et al., 1989a). Comparing the velocity components in the flows beneath the constant and increasing wind, there seems to be a minimal difference at $t = 24.5$ hours, i.e when the increasing wind has reached the same wind speed as the constant wind. At earlier time steps in the simulations there is a difference in the flows beneath a constant and increasing wind in v-direction for strong wind. Apart from this the tidal current seems to dominate the flows in u-direction for both cases, which is also the direction of the tidal forcing, i.e. along the x-axis.

The difference between the particle trajectories beneath a constant and a suddenly increasing wind with tidal forcing, is most significant at the ocean surface. Here, the trajectories due to an increasing wind are consequently shorter compared to constant wind and they are moved less to the right relative to the direction of the wind. This is seen for both strong and weak wind. It appears to be a juggle between the balance of the Coriolis force and the shear force in the start-up of the increasing wind, resulting in a slightly change in the direction of the trajectories compared to the trajectories beneath a constant wind. The change of direction for the trajectories beneath an increasing wind compared to a constant wind is again seen for the direction of the mass transport (drift) in the ocean. Both at the ocean surface and close to the sea bottom the drift due to an increasing wind is rotated less to the right compared to the drift in the flow beneath a constant wind. This may be an effect of higher velocity in the flow beneath a constant wind in

the start-up of the simulation, resulting in the Coriolis force dominating over the shear forces and turning the drift to the right relative to the direction of motion. This was also seen for the particle trajectories at the ocean surface beneath a pure wind flow, and with the presence of a tidal forcing this seems to be valid for the entire water column, even for depth close to the sea bottom. This may be explained by the tidal currents providing mixing in the layer, resulting in little inertia of momentum down in the water column.

In conclusion, the characteristics of an increasing wind on the flow differs compared to those of a constant wind. The presence of a tidal flow results in turbulent mixing which reduces the difference down in the water column due to little inertia of momentum, but e.g. the direction of drift beneath an increasing wind deviates compared to the drift in a flow beneath a constant wind. The results implies that the magnitude and strength of the winds are essential for e.g. the mass transport (drift) in the ocean, despite a dominating tidal current. This may be interesting results since the weather conditions in exposed seas as e.g the North Sea can change suddenly, and the flow beneath a transient wind with sudden change of direction may be more relevant compared to steady state conditions.

Chapter 9

Recommendations for further work

In this thesis the interaction between a tidally driven flow and an increasing wind driven flow has been investigated. In rough seas as e.g. the North Sea the case of a transient and unsteady wind may be of more relevance compared to a constant wind with steady state conditions. Here, only an suddenly linearly increasing wind have been applied to the tidally driven flow. To predict the flow beneath a starting wind more precisely it would be interesting to conduct simulations of a wind increasing e.g. exponentially, or with a varying wind speed and/or a sudden change of direction.

For strong winds blowing over the ocean surface the effect of the wind can extend as far as 100-200 meters down the water column Pinet (2016), resulting in the net mass (water) transport changing direction compared to the current, i.e. the Ekman spiral. The results in this thesis showed that the mass transport (drift) at the ocean surface and at 1 meter above the sea bottom deviates when comparing the tidally driven flow beneath a constant wind with an increasing wind. These results should also be validated by other studies, as this is interesting in order to learn more about the direction of the transport in the ocean. With the increasing challenge of pollution of plastic in the oceans, more knowledge of how the mass transport is affected of various sea states may be important in order to stop this development. In order to perform simulations predicting the effect on a tidally driven flow as a result of an increasing wind in a realistic sea state, contributions from surface waves due to the wind would also be natural to consider.

Bibliography

J. Brown, A. Colling, D. Park, J. Phillips, D. Rothery, and J. Wright. *Waves, Tides and Shallow-water Processes*. The Open University, 1989a.

P.N Brown, G.D. Byrne, and A.C Hindmarsh. Vode: A variable-coefficient ode solver. *SIAM Journal on Scientific and Statistical Computing*, 10(5):1038–1051, 1989b.

B. Cushman-Roisin. *Introduction to Geophysical Fluid Dynamics*. Prentice-Hall,, 1994.

V.W Ekman. On the influence of the earth's rotation on ocean currents. *Arkiv för matematik, astronomi och fysik.*, 2:11, 1905.

O.M Faltinsen. *Sea loads on ships and offshore structures*. Cambridge university press, 1990.

B.R. Grant. *The Oceans and Climate, Second Edition*. The Press Syndicate of The University of Cambridge,, 2003.

C. Haoliang, P. Malanotte-Rizzoli, K. Tieh-Yong, and S. Guiting. The relative importance of the wind-driven and tidal circulations in malacca strait. *Continental Shelf Research*, 88:92–102, 2014.

L. E. Holmedal. *Wave-Current Interactions in the Vicinity of the sea bed. Ph.d.* Norwegian University of Science and Technology, 2002.

L. E. Holmedal and D. Myrhaug. Combined tidal and wind driven flows and bedload transport over a flat bottom. *Ocean Modelling*, 68:37–56, 2013.

A. Johansson. Engineering turbulence models and their development, with emphasis on explicit algebraic reynolds stress models. In M. Oberlack and F.H. Busse, editors, *Theories of Turbulence*, chapter 5, pages 253–300. Springer-Verlag Wien New York, Italy, 2002.

H.L King, A.G Davies, and R.L Soulsby. A numerical model of the turbulent boundary layer beneath surface waves and tides. *Institute of oceanographic science*, 196:90pp, 1985.

G.L Mellor. *Introduction to Physical Oceanography.* Springer-Verlag New York, 1996.

D. Myrhaug. *Oceanography: Wind, Waves.* Marinteknisk senter, Institutt for marin teknikk, 2006.

D. Myrhaug. *Oceanography: Current.* Marinteknisk senter, Institutt for marin teknikk, 2012.

P.R. Pinet. *Invitation to Oceanography, Seventh Edition.* Jones Bartlett Learning,, 2016.

W. Rodi. *Turbulence Models and Their Application in Hydraulics, A state-of-the-art review, Third Edition.* A.A. Balkema Publishers, 1993.

H. Schlichting and K. Gersten. *Boundary Layer Theory.* Springer-Verlag, 2000.

H. Tennekes and J.L. Lumley. *A first course in turbulence.* The Massachusetts Institute of Technology, 1972.

Frank M. White. *Viscous Fluid Flow - Third Edition.* McGraw-Hill Education, 2006.

Appendices

Appendix A

Deducing the Boundary Layer Equations

The thickness of the boundary layer depends on the viscosity of the fluid and the free stream velocity, represented by the Reynolds number. According to Schlichting and Gersten (2000), the boundary layer thickness is proportional to the square root of the kinematic viscosity:

$$\delta \propto \sqrt{\nu}$$

The boundary layer becomes thinner the higher the Reynolds number, and to simplify the Navier-Stokes equations, it can be assumed that the boundary layer thickness is very small compared to the characteristic length of the body (Schlichting and Gersten, 2000)

$$\delta << l$$

This can be implemented to a typical ocean basin. The flow is now the current in the ocean. Here H is the height and L is the length of the basin (Myrhaug, 2012), with typical scales being

$$H \approx 4000m$$

$$L \approx 4000km$$

which gives

$$\frac{H}{L} \approx 10^{-}3 << 1$$

This shows that the vertical scale is much smaller than the horizontal scale. When some terms are much smaller than others, they can be neglected (Myrhaug, 2012). This is used to simplify the Navier-Stokes equations and to deduce the boundary layer equations.

To make the equation non-dimensional, the following relations are used (Myrhaug, 2012):

$$x = \frac{\hat{x}}{L} \iff \hat{x} = x * L$$

$$z = \frac{\hat{z}}{H} \iff \hat{z} = z * H$$

$$u = \frac{\hat{u}}{u_0} \iff \hat{u} = u * u_0$$

where u_0 is the characteristic quantity of u. The time scale is determined as the

$$\frac{lenght - scale}{velocity - scale}$$

which gives

$$t = \frac{\hat{t}}{\frac{L}{u_0}} \iff \hat{t} = t * (\frac{L}{u_0})$$

The vertical velocity-scale is defined similarly

$$\frac{vertcal - lenght}{time - scale}$$

Resulting in

$$w = \frac{\hat{w}}{\frac{H}{\frac{L}{u_0}}} \iff \hat{w} = w * \frac{H}{\frac{L}{u_0}}$$

The pressure is scaled with

$$p = \frac{\hat{p}}{\rho u_0^2} \iff \hat{p} = \rho u_0^2 p$$

These scaled quantities are then plugged into the Navier-Stokes equations. To find out which term is the smallest, the relations

$$H << L$$

$$w << u$$

are used. Inserted in the Navier-Stokes equations for $x_i(i = 1)$ and $u_i(i = 1)$, this gives

$$\frac{u_0^2}{L}\frac{\partial u}{\partial t} + \frac{u_0^2}{L}u\frac{\partial u}{\partial x} + \frac{u_0^2}{L}v\frac{\partial u}{\partial y} + \frac{u_0^2}{L}w\frac{\partial u}{\partial z} = -\frac{u_0^2}{L}\frac{\partial p}{\partial x} + \nu\frac{u_0}{L^2}\frac{\partial^2 u}{\partial x^2} + \nu\frac{u_0}{L^2}\frac{\partial^2 u}{\partial y^2} + \nu\frac{u_0}{H^2}\frac{\partial^2 u}{\partial z^2}$$

Rearranging and multiplying all terms with $\frac{L}{U_0^2}$, the equation becomes

$$\frac{\partial u}{\partial t}+u\frac{\partial u}{\partial x}+v\frac{\partial u}{\partial y}+w\frac{\partial u}{\partial z}=-\frac{\partial p}{\partial x}+\frac{\nu}{u_0L}\frac{\partial^2 u}{\partial x^2}+\frac{\nu}{u_0L}\frac{\partial x^2 u}{\partial y^2}+\frac{\nu}{u_0L}\frac{L^2}{H^2}\frac{\partial^2 u}{\partial z^2}$$

The last term is multiplied with L both over and under the fraction bar, to show that $\frac{\nu}{U_0L}=\frac{1}{Re}$ which for high Reynolds numbers becomes very small. The term $\frac{L^2}{H^2}$ on the other hand is large since $H << L$. Consequently, the term has to remain in the equation since it is unknown whether it will become small or large (Myrhaug, 2012). The terms $\frac{\nu}{u_0L}\frac{\partial^2 u}{\partial x^2}$ and $\frac{\nu}{u_0L}\frac{\partial^2 u}{\partial y^2}$ becomes insignificant for very high Reynolds numbers, and can be neglected. Hence, the boundary layer equation for x-direction reduces to (here u is used for the dimensional components)

$$\frac{\partial u}{\partial t}+u\frac{\partial u}{\partial x}+y\frac{\partial u}{\partial y}+w\frac{\partial u}{\partial z}=-\frac{1}{\rho}\frac{\partial p}{\partial x}+\nu\frac{\partial^2 u}{\partial z^2} \tag{A.1}$$

The result for the y-component of the boundary layer equation is obtained similarly as

$$\frac{\partial v}{\partial t}+u\frac{\partial v}{\partial x}+\frac{\partial v}{\partial y}+\frac{\partial v}{\partial z}=-\frac{1}{\rho}\frac{\partial p}{\partial y}+\nu\frac{\partial^2 v}{\partial z^2} \tag{A.2}$$

The z-component of the boundary layer equation differs from the equations for x and y. Using the same scaling as described above, the equation for the z-component can be written as

$$\frac{Hu_0^2}{L^2}\frac{\partial w}{\partial t}+\frac{Hu_0^2}{L}u\frac{\partial w}{\partial x}+\frac{Hu_0^2}{L}v\frac{\partial w}{\partial y}+\frac{Hu_0^2}{L}w\frac{\partial w}{\partial z}=-\frac{u_0^2}{H}\frac{\partial p}{\partial z}+\nu\frac{Hu_0}{L^3}\frac{\partial^2 w}{\partial x^2}+\nu\frac{Hu_0}{L^3}\frac{\partial^2 w}{\partial y^2}+\nu\frac{u_0}{HL}\frac{\partial^2 w}{\partial z^2}$$

By multiplying all terms with $\frac{L^2}{Hu_0^2}$ the equation becomes

$$\frac{\partial w}{\partial t}+u\frac{\partial w}{\partial x}+v\frac{\partial w}{\partial y}+w\frac{\partial w}{\partial z}=-\frac{L^2}{H^2}\frac{\partial p}{\partial z}+\frac{\nu}{Lu_0}\frac{\partial^2 w}{\partial x^2}+\frac{\nu}{Lu_0}\frac{\partial^2 w}{\partial y^2}+\frac{\nu}{Lu_0}\frac{L^2}{H^2}\frac{\partial^2 w}{\partial z^2}$$

Implementing the assumptions gives $\frac{L^2}{H^2} >> 1$. This term is represented two places in the equation, both for $\frac{L^2}{H^2}\frac{\partial p}{\partial z}$ and $\frac{\nu}{Lu_0}\frac{L^2}{H^2}\frac{\partial^2 w}{\partial x^2}$. As shown earlier, $\frac{\nu}{Lu_0}=\frac{1}{Re}$ and is small for high Reynolds numbers. Since the three last terms on the right hand side of the equations is multiplied with $\frac{\nu}{Lu_0}=\frac{1}{Re}$, they become small. Even the last term will be much smaller than the pressure term, despite the contributions from $\frac{L^2}{H^2} >> 1$. This leads to $-\frac{L^2}{H^2}\frac{\partial p}{\partial z}$ being much larger than all other terms in the equation (Myrhaug, 2012). The boundary layer equation for the z-component therefore reduces to

$$\frac{\delta p}{\delta z}=0 \tag{A.3}$$

Appendix B

Pure Tidally Driven Flow

The one-dimensional boundary layer model developed by Holmedal (2002) is used to predict the pure tidally driven flow over an intermediate water depth, and the results are compared with field measurements in order to validate the model. The horizontal velocities are calculated at 200 grid points in the vertical direction along the water column, with the highest resolution close to the sea bottom where the flow is complex.

The horizontal velocity, u, and the vertical velocity, v, are calculated at 1, 2.5, 15, 30, 50, 70 and 90 meters above the sea bottom, during one tidal cycle. For the simulation, an average bed roughness length of $z_0 = 0.1$ cm is used, with a tidal period of 12.25 hours and a Coriolis parameter $f = 1.112 * 10^{-4}$ per second. The results are compared with field data measured west of the Isles of Scilly in the Celtic Sea in March 1983 by King et al. (1985). The horizontal velocities are measured at 1, 2.5, 15, 30, 50, 70 and 90 meters above the sea bottom. The horizontal velocities of u and v predicted by the model, are presented as tidal time series in figure B.1 and as velocity ellipses in figure B.2. For every elevation the predicted velocity from the model is plotted with the corresponding velocity measured by King et al. (1985) for comparison.

The velocity time series shows a deviation in the phase angle i.e. it is not purely harmonic. This depends on the effects from the Moon and the Sun, and this deviation is as expected when the effects from the Sun is excluded. In the model a free stream velocity measured at 70 meters above the sea bottom is used to find the horizontal pressure gradients which according to the boundary layer approximation is constant through the boundary layer.

There may be an effect of shear stresses from the tidal boundary layer at this height and this may have affected the results. It is also discussed whether the wave conditions during the field measurements conducted by King et al. (1985) could have affected the result.

All in all, the results shows that a relative simple one-dimensional boundary layer model can predict the tidal flow when the turbulence is properly modelled, as in the model used in this paper.

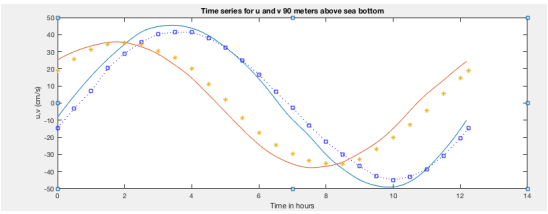

(a) 90 meters above the sea bottom

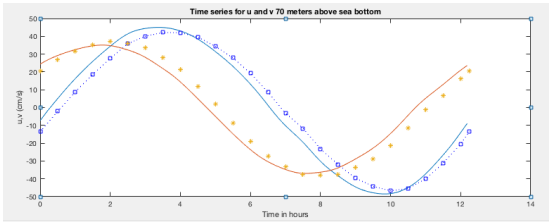

(b) 70 meters above the sea bottom

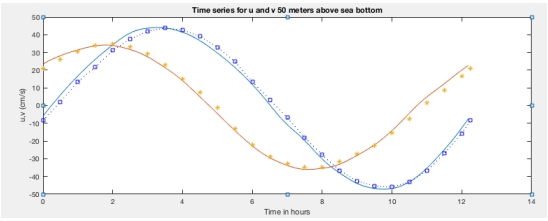

(c) 50 meters above the sea bottom

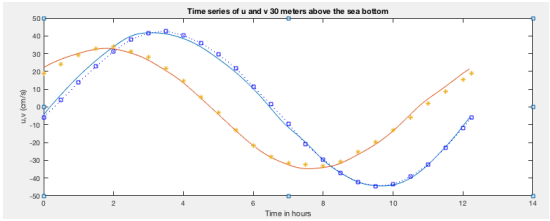

(d) 30 meters above the sea bottom

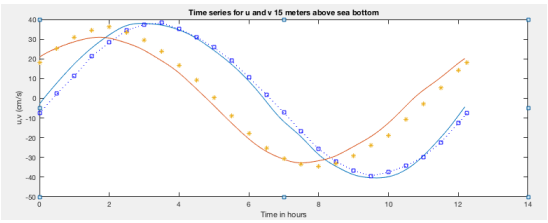

(e) 15 meters above the sea bottom

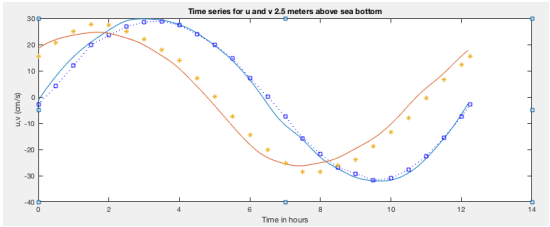

(f) 2.5 meters above the sea bottom

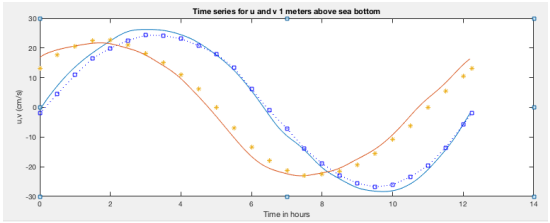

(g) 1.0 meters above the sea bottom

Figure B.1: The tidal time series for different elevations above the sea bottom

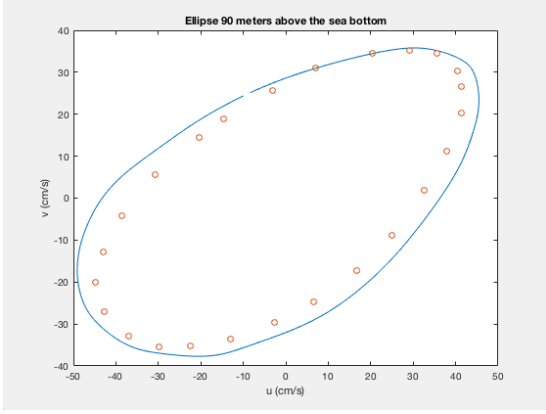

(a) 90 meters above the sea bottom

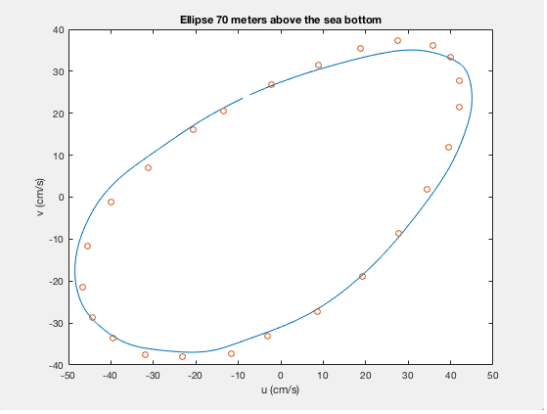

(b) 70 meters above the sea bottom

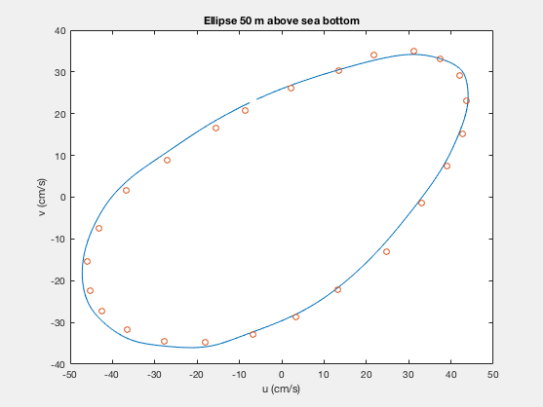

(c) 50 meters above the sea bottom

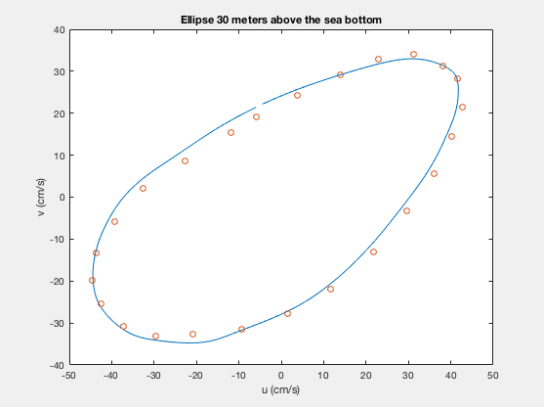

(d) 30 meters above the sea bottom

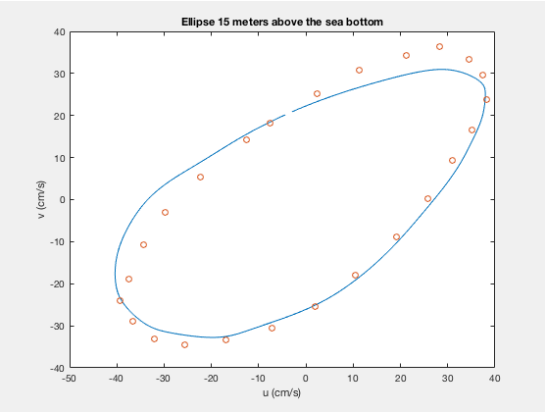

(e) 15 meters above the sea bottom

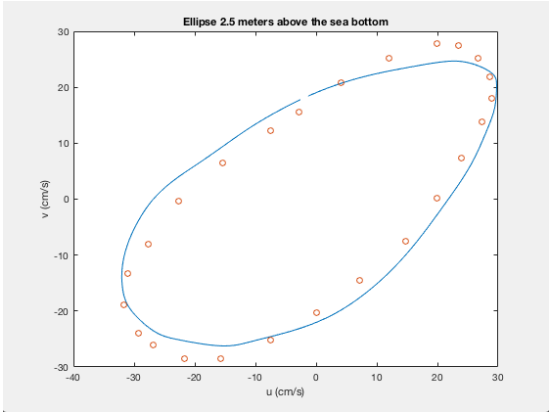

(f) 2.5 meters above the sea bottom

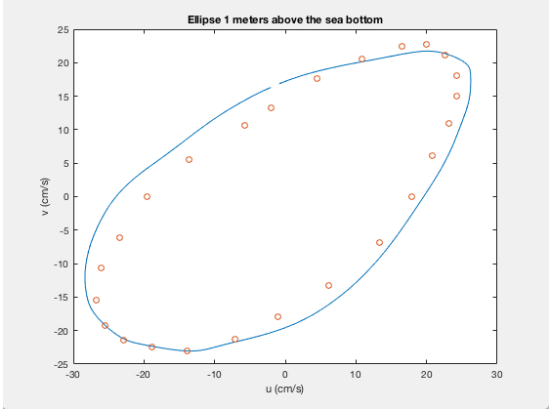

(g) 1.0 meters above the sea bottom

Figure B.2: The tidal velocity ellipses for different elevations above the sea bottom